Elongasome core proteins and class A PBP1a display zonal, processive movement at the midcell of *Streptococcus pneumoniae*

Amilcar J. Perez[a1], Melissa M. Lamanna[a1], Kevin E. Bruce[a1], Marc A. Touraev[a], Julia E. Page[b], Sidney L. Shaw[a], Ho-Ching Tiffany Tsui[a], and Malcolm E. Winkler[a2]

[a]Department of Biology, Indiana University Bloomington, Bloomington, IN 47405; [b]Department of Microbiology, Blavatnik Institute, Harvard Medical School, Boston, MA 02115

[1]A.J.P., M.M.L. and K.E.B. contributed equally to this work.

Running title: Dynamics of pneumococcal peripheral PG synthesis

Key words: processive movement of PG synthesis proteins; PBP2b:RodA:MreC elongasome dynamics; Class A PBP circumferential movement; MpgA muramidase confined subdiffusion; diffusion of non-active PG synthesis proteins

[2]Corresponding author:

Malcolm E. Winkler
Department of Biology
Indiana University Bloomington
1001 East Third Street
Bloomington, Indiana 47405 USA
Phone: 812-856-1318
Email: winklerm@indiana.edu

ABSTRACT

Ovoid-shaped bacteria, such as *Streptococcus pneumoniae* (pneumococcus), have two spatially separated peptidoglycan (PG) synthase nanomachines that locate zonally to the midcell of dividing cells. The septal PG synthase bPBP2x:FtsW closes the septum of dividing pneumococcal cells, whereas the elongasome located on the outer edge of the septal annulus synthesizes peripheral PG outward. We showed previously by sm-TIRFm that the septal PG synthase moves circumferentially at midcell, driven by PG synthesis and not by FtsZ treadmilling. The pneumococcal elongasome consists of the PG synthase bPBP2b:RodA, regulators MreC, MreD, and RodZ, but not MreB, and genetically associated proteins Class A aPBP1a and muramidase MpgA. Given its zonal location separate from FtsZ, it was of considerable interest to determine the dynamics of proteins in the pneumococcal elongasome. We found that bPBP2b, RodA, and MreC move circumferentially with the same velocities and durations at midcell, driven by PG synthesis. However, outside of the midcell zone, the majority of these elongasome proteins move diffusively over the entire surface of cells. Depletion of MreC resulted in loss of circumferential movement of bPBP2b, and bPBP2b and RodA require each other for localization and circumferential movement. Notably, a fraction of aPBP1a molecules also moved circumferentially at midcell with velocities similar to those of components of the core elongasome, but for shorter durations. Other aPBP1a molecules were static at midcell or diffusing over cell bodies. Last, MpgA displayed non-processive, subdiffusive motion that was largely confined to the midcell region and less frequently detected over the cell body.

SIGNIFICANCE

This paper reports three types of single-molecule motions of PG synthesis proteins in the ovoid-shaped, pathogenic bacterium *Streptococcus pneumoniae*, not reported previously in other bacteria. The core elongasome exhibits zonal, circumferential motion in the absence of MreB filaments, independent of FtsZ treadmilling or the processive movement of the septal PG synthase. Class A aPBP1a also moves processively at midcell, but is not a persistent component of the core elongasome. These types of motions have implications for the functions of these PG synthases and indicate that processive motion in pneumococcus follows spatially separate tracks, possibly reflective of PG structure. In contrast, the MpgA muramidase displays a different kind of subdiffusive motion that is largely confined to midcell by an unknown mechanism.

INTRODUCTION

The peptidoglycan (PG) cell wall protects bacteria from osmotic stress, determines cell shape, size, and chaining critical for adaptation and host interactions, and serves as a scaffolding in Gram-positive bacteria for the attachment of wall-teichoic acids, capsules, and extracellular enzymes and virulence factors (1-5). PG synthesis has provided targets for a large number of clinically relevant antibiotics and remains one of the most fertile sources for the discovery of new antibiotic targets in drug-resistant pathogens (6-11). Although a general picture of PG synthesis has emerged (12-16), many fundamental questions remain unanswered about the composition, coordination, chronology, and regulation of the nanomachines that carry out PG synthesis in bacteria. Moreover, major differences have recently emerged in how different bacteria carry out PG synthesis and

use homologous proteins in different ways (see (17-23)). *Streptococcus pneumoniae* (pneumococcus; *Spn*) has emerged as a model for PG synthesis in ovoid-shaped bacteria that is tractable to genetic, biochemical, and cell biological approaches (reviewed in (4, 24, 25)). *S. pneumoniae* is a human nasopharyngeal commensal bacterium that becomes a serious opportunistic pathogen, killing over one million people annually worldwide (26-28). Moreover, *S. pneumoniae* is an antibiotic-resistant "superbug," for which new antibiotic targets are urgently needed (10, 29-31).

Unlike in rod-shaped bacteria, all PG synthesis is zonal and confined to a band at the middle of dividing *S. pneumoniae* cells (Fig. S1) (24, 32, 33). At the start of cell division, the septal and elongation (peripheral) PG synthesis nanomachines locate to an FtsZ ring at the equators of predivisional daughter cells (Fig. S1*A*) (34, 35). Unlike *Bacillus subtilis* and *Staphylococcus aureus* (36-39), septal ring closure and cell separation occur simultaneously during the *S. pneumoniae* cell cycle, as do septal and elongation PG synthesis, with elongation PG synthesis likely starting slightly before septal PG synthesis in the initial FtsZ ring (24, 32, 33, 35, 40). As septation progresses, the septal and elongation PG synthesis nanomachines physically separate to the inside and outside edges, respectively, of the midcell annular disk (Fig. S1*B* and S1*C*) (24, 33, 41). Septal PG synthesis in the inner ring, which contains FtsZ and the Class B bPBP2x:FtsW (SEDS) complex, separates the dividing cells (24, 32-35). Elongation PG synthesis, which is carried out by the pneumococcal core elongasome in the outer ring (24, 32, 33), emanates outward and has been postulated to push MapZ-nascent FtsZ/FtsA/EzrA rings toward the equators of new daughter cells (Fig. S1*A*) (34, 42, 43). Notably, *S. pneumoniae* lacks Min and Noc systems (44, 45) and forms FtsZ rings over the nucleoid (22, 46, 47).

97 Consequently, dividing pneumococcal cells characteristically contain three FtsZ rings
98 throughout most of division, one at the closing septum and two in the developing
99 equatorial rings (Fig. S1*A*) (34, 46, 48). Interestingly, proteins that mediate bundling FtsZ
100 filaments, such as SepF, ZapA, and ZapJ (ZipA is absent), arrive to the equatorial rings
101 very late in cell division (34, 41, 49).

102 Septal ring closure is zonal and confined to a midcell ring in many bacteria (50-52).
103 Dynamics studies showed that the pneumococcal bPBP2x:FtsW PG septal synthase
104 moves circumferentially at midcell driven by PG synthesis itself, and not by FtsZ
105 treadmilling (34), as was initially concluded for *B. subtilis* (53). Recent papers
106 demonstrate that zonal septal closure is indeed driven by circumferential septal PG
107 synthesis in *Escherichia coli* (54), *S. aureus* (55), and *B. subtilis* (56), rather than by FtsZ
108 treadmilling.

109 However, elongation PG synthesis in rod-shaped cells is not zonal but is distributed
110 along the curved cylindrical body of growing cells (57-59). This synthesis is carried out by
111 the Rod-complex elongasome consisting of MreB and the PG elongasome complex.
112 Actin-like MreB polymerizes into multiple short, curved filaments perpendicular to the cell
113 long axis along the cell membrane, which is the region of maximal negative Gaussian
114 curvature (16, 60-62). MreB interacts with the cytoplasmic helix-turn-helix domain of the
115 bitopic RodZ protein that also interacts with the elongasome PG synthase complex facing
116 outside the cell membrane (62-65). The core elongasome consists of the polytopic shape,
117 elongation, division and sporulation (SEDS) family protein RodA (glycosyltransferase;
118 GT), an essential bitopic Class B bPBP (transpeptidase; TP), and bitopic and polytopic
119 positive regulators MreC and MreD, respectively (16, 66-70). Similar to septal PG

synthesis, movement of the assembled Rod elongasome is driven by side-wall PG synthesis itself, rather than by ATPase-dependent treadmilling of MreB (57-59). Thus, MreB filaments serve as curvature-sensing “rudders” for processive synthesis of separate parallel strands of side-wall PG (61). In addition, Class A PBPs, which are bitopic proteins with extracellular GT and TP activities, move largely in non-ordered paths and often stop, possibly filling in or reinforcing gaps left by the Rod system (16, 71-74).

In contrast to rod-shaped bacteria, pneumococcal elongasome PG synthesis is zonal and confined to the initial FtsZ ring and later to the outer edge of the septal annular disk (24, 32, 33). The core pneumococcal elongasome contains RodA, Class B bPBP2b, RodZ, MreC, and MreD, but does not contain an MreB homolog (19, 25, 35, 46, 75-79). RodZ(*Spn*) serves as an organizer of elongasome assembly and is required for MreC midcell localization followed by localization of RodA and bPBP2b (19, 80).

Immunofluorescence microscopy (IFM) indicated that bPBP2b, MreC, and RodZ co-localize throughout the cell cycle at midcell and localize in middle-to-late divisional cells to a larger ring than FtsZ and bPBP2x, the TP in septal PG synthesis (19, 35, 46). This larger ring corresponds to the outer elongasome PG synthesis ring observed at midcell (Fig. S1). Direct evidence for this conclusion came from examination of FDAA-labeled vertically oriented cells by high-resolution 3D-SIM (32). bPBP2x and bPBP2b engaged in PG synthesis localized initially with FtsZ to the equatorial ring of pre-divisional cells. Later in division, bPBP2x and FtsZ located primarily to the inner FDAA-labeled ring at midcell, while bPBP2b located to the outer ring (32). Given that the synthetically active elongasome complex contains a complex of bPBP2b, RodA, MreC complex in *S. pneumoniae* (16, 19), it is presumed here that active RodA at midcell locates to the FtsZ

143 ring early in division and to the outer midcell ring later in division, similar to bPBP2b and
144 MreC. IFM also indicated that Class A aPBP1a and the MpgA muramidase co-localize
145 with bPBP2b and MreC, but not with bPBP2x, throughout the cell cycle, including to the
146 outer midcell ring later in division (Fig. S1) (35, 46, 80). In addition, interactions were
147 detected between aPBP1a and MpgA and components of the elongasome, including
148 RodZ and MreC (19). Thus, aPBP1a and MpgA localize with peripheral PG synthesis,
149 although it has not been determined whether they are persistent members of the core
150 elongasome.

151 Paradoxically, the absence of aPBP1a suppresses the requirement for MreCD and
152 RodZ (80, 81), whereas inactivation of *pbp1b*, which encodes Class A aPBP1b,
153 suppresses the requirement for RodZ, but not for MreCD (19). In both cases, the
154 bPBP2b:RodA PG synthase is still required for viability, suggesting that the absence of
155 aPBP1a or aPBP1b may activate bypass pathways that obviate the requirement for
156 certain regulators of the core elongasome (19, 80). However, amino acid changes that
157 reduce the catalytic activity of the MpgA muramidase (80, 82) abolish the requirement for
158 the entire pneumococcal PG elongasome, including the bPBP2b:RodA PG synthase (24,
159 80). The CozE protein was also implicated in pneumococcal elongation PG synthesis
160 (83). However, CozE did not behave equivalently to MreCD in transformation assays of
161 function (84), and the exact function of pneumococcal CozE remains unknown. A
162 pneumococcal TseB homolog renamed as CopD was recently reported to bind to bPBP2b
163 and aPBP1a. Absence of CopD produces wider cells, consistent with a defect in
164 elongation PG synthesis (85); however, the mechanism underlying this morphology
165 change is not known. Last, FtsX is located with the outer ring elongasome proteins later

166 in pneumococcal division (32). FtsX is a subunit of the FtsEX:PcsB PG hydrolase that is
167 thought to play an essential role in PG remodeling between septal and peripheral PG (86-
168 89). Notably, the FtsX(*Bsu*) homolog is also associated with side-wall PG synthesis (90,
169 91).

170 In this paper, we show that the pneumococcal bPBP2b, RodA, and MreC core
171 elongasome proteins move circumferentially with the same velocity and processivity at
172 midcell at different division stages. Unless indicated otherwise, midcell refers to the
173 central rings at the septa of dividing cells and to the equators of predivisional daughter
174 cells about to start division. The processive movement of the core elongasome
175 components is driven by PG synthesis, and is not affected by FtsZ treadmilling, consistent
176 with the absence of FtsZ in the outer ring of elongasome PG synthesis later in division.
177 Strikingly, at WT protein expression levels in exponentially growing cells, a large majority
178 of bPBP2b, RodA, and MreC molecules diffuse in the membrane over the body of
179 pneumococcal cells without synthesizing PG. Unexpectedly, Class A aPBP1a also moves
180 circumferentially at midcell with a similar velocity, but in shorter tracks, than the core
181 elongasome components. Processive movement of aPBP1a at midcell depended on PG
182 synthesis, and again, a majority of aPBP1a molecules were found diffusing over the cell
183 body without synthesizing PG. Finally, the MpgA muramidase showed a distinctive
184 pattern of non-processive, subdiffusive movement, largely confined to midcell regions.
185 These results demonstrate that the pneumococcal PG elongasome moves zonally, which
186 is different from elongasome movement in rod-shaped bacteria, that a Class A PBP
187 moves circumferentially as well as diffusively, and that a PG hydrolase shows unusual
188 fast non-processive movement confined largely to the midcell region. The implications of

these modes of movement to the functions of the pneumococcal PG elongasome, Class A PBPs, and PG muramidases and to patterns of PG-glycan strand placement are discussed.

RESULTS

Construction of functional fluorescent-protein fusions. Fusions to pneumococcal elongasome proteins bPBP2b, RodA, MreC, aPBP1a, and MpgA, were constructed at native chromosomal loci to contain an N-terminal expression-enhancing “i-tag”, fused to an intracellular HaloTag (HT) domain, followed by a 15 amino-acid linker, fused to the protein of interest (Tables S1 and S2), as described previously (32, 34, 92-95). Growth of strains expressing iHT-fused proteins in C+Y, pH 6.9 medium was indistinguishable from that of WT (Fig. S2*A*). Localization of iHT-fused proteins labeled with saturating amounts of HT-TMR ligand matched previously published localization patterns of epitope-tagged or GFP-fused proteins imaged by IFM or two-dimensional epifluorescence microscopy (2D-FM), respectively (Fig. S2*B*) (19, 32, 34, 35, 42, 46, 80, 81, 85, 96). Western blots of these fusions with intracellular iHT domains probed with antibody to native MreC, bPBP2b, aPBP1a, or MpgA showed expression of full-length fusions with minimal cleavage of the iHT domain (Fig. S3*A*, S4*B*, S5*B*, and S6). In contrast, western blots of an extracellular C-terminal HT fusion to MreC (MreC-HT) probed with anti-MreC antibody showed extensive cleavage of the HT domain not detectable in blots probed with anti-HT antibody (Fig. S3*A*, middle and right). Cleavage of extracellular HT domains was also reported in *E. coli* (97), and our results emphasize the need to validate protein fusion stability in blots with antibody to native proteins.

212 We reported previously that some tagged proteins, such as iHT-bPBP2b and sfGFP-
213 bPBP2b, were expressed from their chromosomal locus in significantly lower amounts
214 than WT bPBP2b in cells grown in BHI broth, with only minor effects on cell growth and
215 morphology under this growth condition (32). We observed similar results for cells grown
216 in C+Y, pH 6.9 medium, which is utilized in live-cell fluorescence microscopy due to low
217 levels of autofluorescence (34). The cellular amounts of iHT-bPBP2b and iHT-aPBP1a
218 were 15 ± 5% and 10 ± 10% (mean ±SD) of the WT bPBP2b and aPBP1a amounts,
219 respectively (Fig. S4*B* and S5*B*; Table S3). Underproduced iHT-bPBP2b caused minor
220 increases in cell width and size (Fig. S4*C* and S4*D*). However, the reduced amount of
221 iHT-aPBP1a caused decreased cell width, which phenocopied a Δ*pbp1a* mutant (Fig.
222 S5*C* and S5*D*) (81). The cellular amounts of iHT-MreC and iHT-MpgA expressed from
223 their chromosomal loci were 82 ±18% and 171 ± 11% of the WT MreC and MpgA
224 amounts, respectively (Fig. S3*A* and S6; Table S3). Cells expressing iHT-MreC showed
225 minimal cell morphology differences from WT (Fig. S2*B* and S3*B*).

226 To increase cellular amounts of iHT-bPBP2b, iHT-aPBP1a, and iHT-RodA (antibody
227 to native RodA was not available), we constructed merodiploid strains in which each iHT-
228 tagged protein was also expressed from an ectopic site under the control of a zinc-
229 inducible promoter (98). Addition of Zn inducer ([$ZnCl_2$] indicated + 1/10 [$MnSO_4$] to
230 reduce zinc toxicity (41, 80, 99)) to cultures of these merodiploid strains did not affect
231 growth (Fig. S4*A* and S5*A*). Zn addition complemented the low cellular amounts of iHT-
232 bPBP2b and iHT-aPBP1a back up to 82 ± 6% and 101 ± 41% of the WT bPBP2b and
233 aPBP1a amounts, respectively (Fig. S4*B* and S5*B*; Table S3). Complementation also
234 alleviated minor cell shape defects detected in strains with reduced protein amounts (Fig.

235 S4*C*, S4*D*, S5*C*, S5*D*, and S7). iHT-fused proteins localized strongly to midcell of Zn-
236 induced merodiploid strains, but were also more dispersed over bodies of cells compared
237 to haploid or uninduced merodiploid strains (Fig. S4*C* and S5*C*). Finally, merodiploid
238 strains expressing iHT-bPBP2b or iHT-RodA showed minimal amounts of cleavage
239 products when 0.2 mM or 0.25 mM Zn inducer was added to the growth medium (Fig.
240 S4*B* and S7*B*). Effects of protein amounts on dynamics are described below.

241 **bPBP2b, RodA, and MreC display similar processive circumferential motion at**
242 **midcell.** Strains expressing functional iHT-fused proteins were labeled with limiting
243 concentrations of HT-JF549 ligand (Table S4), and single-molecule total internal
244 reflection fluorescence microscopy (sm-TIRFm) was performed for 180 s, as described
245 previously (34) (*Materials and Methods*). *S. pneumoniae* division is highly regular with
246 septal and equatorial FtsZ-rings forming perpendicular to the long axis at the geometric
247 centers of ovoid-shaped cells (Fig. S*1*). Midcell regions were considered to be within 125
248 nm of geometric centers. Three criteria were used to determine different motion types.
249 Processive circumferential motion was defined as a molecule moving in one direction for
250 more than six consecutive frames (imaging rate = 1 frame per second (FPS)), with a linear
251 velocity of ≥ 5 nm/s determined by kymograph analysis (Fig. 1*A*; *Materials and Methods*).
252 Static molecules were defined as being visible for more than six consecutive frames with
253 a velocity < 5 nm/s. Diffusively moving molecules were defined as moving, but not in a
254 consistent direction, for 6 or more non-consecutive frames within a period of 90 s.

255 Single molecules of iHT-bPBP2b, iHT-RodA, and iHT-MreC displayed similar
256 processive circumferential motion exclusively at midcell (Fig. 1*A* and S8; Movies S1 to
257 S3), that resembled the circumferential motion of iHT-bPBP2x and FtsW-HT reported

258 previously (34). The frequency of circumferential, static, and diffusive molecules was
259 compiled for each strain (Fig. 1*B*). Examination of the circumferential tracks showed that
260 73% (54/74) of iHT-bPBP2b and 74% (57/77) of iHT-MreC molecules moved
261 unidirectionally at midcell. The remaining 27% of iHT-bPBP2b or 26% of iHT-MreC
262 molecules moved in one direction for at least six consecutive frames and then reversed
263 direction and moved in the opposite direction for at least six frames at approximately the
264 same velocity (angle in kymograph; Fig. 1*A*, right). Slow or non-moving static molecules
265 were mainly detected at midcell (Fig. S8), whereas diffusive molecules displayed rapid,
266 erratic movement throughout the cell (Fig. 1*B*; S8; Movies S1 to S3). Fewer than 5% of
267 molecules of these core elongasome proteins were observed to transition between
268 movement states (e.g., static to diffusive or circumferential).

269 **A limited number of bPBP2b, RodA, and MreC molecules engage in active PG**
270 **synthesis.** The distribution of single-molecule movement states of iHT-bPBP2b and iHT-
271 RodA was highly dependent on cellular protein levels. When expressed at 15% of the WT
272 level, ≈60% of iHT-bPBP2b moved circumferentially and only 32% moved diffusively (Fig.
273 1*B*; Movie S1). The remaining 7% of iHT-bPBP2b molecules were static, mainly at
274 midcell. iHT-RodA molecules expressed from the native locus showed a similar
275 distribution, suggesting that iHT-RodA was underproduced (Fig. 1*B*; Movie S2). However,
276 when iHT-PBP2b and iHT-RodA protein amounts were increased by ectopic expression
277 (to ≈82% the WT level for iHT-bPBP2b), only 16% or 9% of single iHT-bPBP2b or iHT-
278 RodA molecules, respectively, moved circumferentially, while ≈70% moved diffusively,
279 with the remaining 12% iHT-bPBP2b or 23% iHT-RodA static, mostly at midcell (Fig. 1*B*;
280 Movies S4 and S5). Uninduced merodiploid strains expressing iHT-bPBP2b or iHT-RodA

281 displayed movement distributions similar to those of haploid strains (Fig. 1*B*). The amount
282 iHT-MreC expressed from its native locus was nearly (82%) that of WT (Fig. S3*A*; Table
283 S3). Approximately 24% of iHT-MreC molecules moved circumferentially, while 52%
284 moved diffusively and 24% were static, similar to the movement distributions of iHT-
285 bPBP2b and iHT-RodA when they were ectopically expressed (Fig. 1*B*; Movie S3).

286 High-resolution 3D structured-illumination microscopy (3D-SIM) on fixed cells
287 corroborated conclusions based on movement distributions. At protein amounts
288 corresponding to ≈15% of WT, iHT-bPBP2b localized primarily to regions of active PG
289 synthesis at midcell and equators of dividing cells, as indicated by HADA fluorescent D-
290 amino-acid labeling (Fig. 2*A*). When expressed near the WT level, iHT-bPBP2b remained
291 at the HADA-labeled midcell and equators but was mostly dispersed over the body of the
292 entire cell where HADA labeling was not detected (Fig. 2*B*). These results support the
293 conclusion that iHT-PBP2b molecules that move diffusively in the cell membrane outside
294 of midcell and equators are not actively synthesizing PG (Fig. 2*B*). Control experiments
295 using a GFP fusion construct to bPBP2b and labeling with a different fluorescent D-amino
296 acid (TADA) gave similar results (Fig. S9). 2D-FM images also showed an increase in
297 dispersed iHT-bPBP2b localization when protein expression was increased to near the
298 WT amount (Fig. S4*C*). We conclude that at any given time, a limited number of bPBP2b,
299 RodA, and MreC molecules display processive circumferential motion at midcell where
300 PG synthesis occurs. Conversely, bPBP2b, RodA, and MreC are expressed in excess in
301 WT cells, and most molecules are diffusing over the cell surface and not synthesizing PG
302 in cells under these and other growth conditions (Fig. 1*B,* 2*B,* and S4*C*; Table S3) (32).

303 **bPBP2b, RodA, and MreC form a stable elongasome complex that undergoes**
304 **circumferential motion.** If bPBP2b, RodA, and MreC form an elongasome complex, we
305 would expect that each molecule would move with the same velocity. To test this idea,
306 velocities of circumferentially moving molecules were determined by kymograph analysis
307 (Fig. 3*A*) (34). The length of time these molecules were observed moving
308 circumferentially, referred to here as the circumferential duration, was also measured
309 (Fig. 3*B*), and the particle distance each circumferential molecule moved was calculated
310 by multiplying the velocity by the duration (Fig. S10*A*). When expressed near WT levels
311 (+Zn in merodiploid and haploid *mreC* constructs) the mean circumferential velocities,
312 durations, and particle distances of iHT-bPBP2b, iHT-RodA, and iHT-MreC were
313 statistically the same, at ≈11 nm/s, ≈23 s, and ≈230 nm, respectively (Fig. 3*A,* 3*B*, and
314 S10*A*). Additional strains containing different fusion constructs of bPBP2b or RodA moved
315 at similar circumferential velocities (Fig. S11). These data support the idea that bPBP2b,
316 RodA, and MreC form a stable, circumferentially moving elongasome complex at midcell.
317 **Circumferential movement of bPBP2b and RodA is independent of FtsZ**
318 **treadmilling and driven by PG synthesis.** Circumferential movement of the
319 pneumococcal septal PG synthase was shown to be independent of FtsZ treadmilling and
320 driven by PG synthesis (34). A similar conclusion was later reported for the septal PG
321 synthases of *S. aureus* (55) and *B. subtilis* (56) and for the population of active septal PG
322 synthases in *E. coli* (54, 100). In early divisional cells, the pneumococcal PG elongasome
323 is located in an FtsZ-ring that also contains the septal PG synthase (Fig. S1*A*), whereas
324 at later stages of division, the elongasome separates from the FtsZ-ring and locates to
325 the outer edge of the septal annular disk (Fig. S1*B* and S1*C*) (24, 32, 33). Notably, the

326 same circumferential velocity of core elongasome protein iHT-MreC, which was
327 expressed near the WT level (Fig. S3*A*), was detected at equators of early divisional cells,
328 before ostensible constriction, and in later-divisional cells with clear constrictions, when
329 septal (inner) and elongasome (outer) rings are separated at midcell (32) (Fig. S1*B* and
330 S10*B*). Since the pneumococcal PG elongasome is initially in an FtsZ ring, we tested
331 whether iHT-bPBP2b velocity is decreased when FtsZ treadmilling is greatly reduced by
332 ectopic expression of GTPase mutant FtsZ(D214A), which reduces FtsZ treadmilling
333 velocity from ≈32 nm/s to ≈4 nm/s (34). To the contrary, overproduction of FtsZ(D214A)
334 caused a statistically minimal increase in iHT-bPBP2b velocity (Fig. 4*A*; Movie S6), with
335 a marginal decrease in growth rate (Fig. S12). Consistent with a lack of dynamic coupling,
336 the treadmilling velocity of FtsZ-sfGFP filaments was ≈2.4-fold greater than the
337 circumferential velocity of iHT-bPBP2b single molecules expressed in the same cell (Fig.
338 4*B*; Movie S7). We conclude that circumferential movement of the pneumococcal PG
339 elongasome is independent of FtsZ treadmilling.

340 Two lines of evidence indicate that pneumococcal PG elongasome circumferential
341 movement is driven by PG synthesis. First, we determined iHT-bPBP2b or iHT-RodA
342 circumferential velocity in a Δ*murZ* (previously called Δ*murA1*) mutant, which lacks the
343 predominant MurZ homolog that catalyzes the first committed step of PG precursor
344 synthesis (34, 101). The circumferential velocity of iHT-bPBP2b or iHT-RodA was
345 substantially reduced by ≈1.6-fold in the Δ*murZ* mutant compared to WT (Fig. 4*C* and 4*D;*
346 Movies S8 and S9). Previously, we showed that the velocity of FtsZ treadmilling is
347 unchanged in the Δ*murZ* mutant (34). Together, these results demonstrate that the rate
348 of midcell elongasome movement is dependent on PG synthesis precursor amounts.

349 Second, catalytic mutants of bPBP2b TP or RodA GT activity did not exhibit
350 processive, circumferential movement. No β-lactam antibiotic is known that preferentially
351 inhibits bPBP2b alone (102). Both bPBP2b and RodA are essential in *S. pneumoniae* (35,
352 75, 103). Consequently, we constructed merodiploid strains with *iht-pbp2b*(S391A) (TP
353 catalytic mutation) or *iht-rodA*(D283A) (GT catalytic mutation) (69) at chromosomal native
354 sites and *pbp2b*$^+$ or *rodA*$^+$ under the control of the zinc-inducible promoter (P_{Zn}) in an
355 ectopic site (Fig. S13*A*). The merodiploid strains were constructed and grown in the
356 presence of Zn inducer, which was removed to deplete the WT proteins (Fig. S13*B*).
357 Interestingly, we were able to construct a *rodA*(D283A)//P_{Zn}-*rodA*$^+$ strain, but we were
358 unable to construct a *pbp2b*(S391A)//P_{Zn}-*pbp2b*$^+$ strain in the presence of Zn inducer.
359 This result suggested that *pbp2b*(S391A) was dominant-negative to WT *pbp2b*$^+$. The
360 reason we were able to construct the *iht-pbp2b*(S391A)//P_{Zn}-*pbp2b*$^+$ merodiploid was the
361 low (≈15%) intrinsic expression of iHT-bPBP2b compared to WT bPBP2b (Fig. S4*B*).
362 Consistent with a dominant-negative effect, depletion of WT bPBP2b in the *iht-*
363 *pbp2b*(S391A)//P_{Zn}-*pbp2b*$^+$ merodiploid resulted in a more severe drop in OD_{620} than in
364 Δ*pbp2b*//P_{Zn}-*pbp2b*$^+$ (Fig. S13*B*), possibly due to the toxicity of uncrosslinked PG
365 produced from GT activity without TP activity (104). Western blot analysis confirmed that
366 both iHT-bPBP2b(S391A) and iHT-RodA(D283A) were expressed and stable relative to
367 iHT-bPBP2b$^+$ and iHT-RodA$^+$, respectively (Fig. S14*A*), and that bPBP2b$^+$ expressed
368 from the ectopic locus was fully depleted after 3h (Fig. S14*B*).

369 No midcell circumferential movement of iHT-bPBP2b(S391A) was detected in the
370 presence or absence of WT bPBP2b (Fig. S13*C*; Movies S10 and S11). Instead, iHT-
371 bPBP2b(S391A) was static at midcell (Fig. S13*D*) or was detected diffusing over the body

372 of cells (Fig. S13*C*). Likewise, no midcell circumferential movement of iHT-RodA(D283A)
373 was detected in the absence of RodA$^+$ (Fig. S13*C*; Movie S12). Like iHT-bPBP2b(S391A),
374 iHT-RodA(D283A) was static at midcell (Fig. S13*D*) or diffusing over the body of cells
375 (Fig. S13*C*). Notably, both iHT-bPBP2b(S391A) and iHT-RodA(D283A) located to midcell
376 (Fig. S13*E*), indicating that catalytic activity was not required for normal localization. From
377 these combined results, we conclude that processive, circumferential movement of the
378 pneumococcal elongasome PG synthase is driven by PG synthesis, but not by FtsZ
379 treadmilling, even in predivisional cells.

380 **bPBP2b localization becomes diffuse and circumferential movement is lost**
381 **when MreC is depleted.** We reported previously that the pneumococcal PG elongasome
382 is assembled sequentially (19). RodZ directs localization of MreC, which then directs
383 localization of the bPBP2b:RodA synthase. In agreement with this conclusion, iHT-
384 bPBP2b localization became diffuse when MreC was depleted (Fig. S15*A*). In addition,
385 there was a large (≈30-fold) drop in the number of iHT-bPBP2b molecules moving
386 circumferentially when MreC was depleted (Fig. S15*B*; Movie S13). Growth curve
387 analysis confirmed reduced growth yield of cells depleted for MreC (Fig. S16*A*), and
388 western blots confirmed the presence of iHT-bPBP2b during MreC depletion (Fig. S16*B*
389 and S16*C*). We conclude that MreC is required for proper midcell localization and for
390 elongasome PG synthesis by the bPBP2b:RodA synthase. This result is consistent with
391 the previous conclusion that MreC allosterically activates the GT/TP activity of
392 RodA:PBP2 in the PG elongasome of *E. coli* (16, 67, 105).

393 **bPBP2b and RodA require each other for localization.** We further tested whether
394 RodA was required for bPBP2b localization, and *vice versa*. Indeed, upon RodA

395 depletion, iHT-bPBP2b went from locating primarily to midcell to being distributed at
396 midcell and over the surface of rounded cells (Fig. S17*A* and S18*C*), indicative of loss of
397 peripheral PG synthesis (35, 75, 81). Additionally, a growth yield phenotype was observed
398 at 4 to 5 h into depletion (Fig. S18*A* and S18*B*). Upon bPBP2b depletion to ≈6% of WT
399 after 3 h (Fig. S14*B*), iHT-RodA also relocated primarily from midcell to being distributed
400 at midcell and over the surface of rounded cells, with a similar reduction in growth yield
401 (Fig. S17*B* and S18). Therefore, there is an interdependence for normal localization of
402 bPBP2b and RodA in the pneumococcal PG elongasome.

403 We next determined the dynamics of iHT-bPBP2b upon depletion of RodA or iHT-
404 RodA upon depletion of bPBP2b. In both cases, the motion distribution shifted from
405 primarily circumferential (≈59%) to diffusive (≈65%) movement (Fig. S17*C*; Movies S14
406 and S15), where iHT-bPBP2b and likely iHT-RodA were underproduced in these stains
407 (Fig. 1*B,* S7, and S14*B*). Remaining circumferential movement at the midcell (≈24% of
408 molecules) likely reflected bPBP2b:RodA complexes that assembled before depletion
409 occurred. Consistent with this interpretation, the velocity of circumferentially moving
410 proteins was unchanged by depletion of its cognate partner (Fig. S17*D* and S17*E*). These
411 data support the idea that when bPBP2b or RodA is depleted, its unpaired cognate
412 partner stops elongation PG synthesis at midcell and is released to diffuse over the cell
413 body. Notably, released, unpaired iHT-bPBP2b or iHT-RodA did not move
414 circumferentially at an increased velocity, suggesting that FtsZ filament end-tracking does
415 not occur for these proteins (100).

416 **aPBP1a displays circumferential dynamics at midcell driven by PG synthesis**
417 **but is not persistently part of the elongasome.** Molecules of iHT-aPBP1a

418 unexpectedly displayed circumferential, as well as diffusive and static dynamics (Fig. 1*A*
419 and 1*B*; Movies S16 to S18). Like iHT-bPBP2b and likely iHT-RodA, iHT-aPBP1a was
420 underproduced in the haploid strain and required ectopic expression to reach or surpass
421 WT levels (Fig. 1*B* and S5*B*). However, in contrast to core elongasome components, the
422 relative frequency of circumferentially moving iHT-aPBP1a molecules (≈10%) was largely
423 independent of protein expression level (Fig. 1*B*), and a high percentage (>60%) of iHT-
424 aPBP1a molecules moved diffusively, even at low expression levels (Fig. 1*B* and S5*B*;
425 Table S3).

426 The mean circumferential velocity of iHT-aPBP1a expressed near WT levels was ≈15
427 nm/s, which was similar to, if not somewhat faster than, that of iHT-bPBP2b, iHT-RodA,
428 and iHT-MreC (≈11 nm/s) (Fig. 1*A* and 3*A*). Strikingly, the mean circumferential duration
429 of iHT-aPBP1a molecules was ≈10 s, more than two-fold shorter than that of iHT-bPBP2b,
430 iHT-RodA, or iHT-MreC (≈23 s) (Fig. 1*A* and 3*B*). Altogether, these results indicate that
431 circumferential motion of aPBP1a is distinct from that of bPBP2b, RodA, and MreC,
432 suggesting that aPBP1a is not persistently part of the core elongasome complex,
433 although shorter interactions are still possible.

434 To confirm that circumferential movement of iHT-aPBP1a molecules depends on PG
435 synthesis, we constructed an *iht-pbp1a*(S370A)//P_{Zn}-*iht-pbp1a*(S370A) merodiploid strain
436 expressing catalytically inactive (TP null) iHT-aPBP1a(S370A) from both the native site
437 and ectopic locus (Table S1). The growth rate of the catalytically inactive iHT-
438 aPBP1a(S370A) merodiploid strain was reduced slightly (≈1.3-fold) when Zn inducer was
439 added to the growth medium (Fig. S19*A*), but protein expression and localization were
440 comparable to that of iHT-aPBP1a merodiploid strains (Fig. S19*B* and S19*C*).

441 Circumferential, diffusive, and static molecules were sorted by cellular location into
442 midcell or locations other than midcell (non-midcell) (Fig. 5). Circumferential movement
443 of iHT-aPBP1a decreased substantially from a relative frequency of ≈21% for iHT-
444 aPBP1a to a marginal ≈3% for iHT-aPBP1a(S370A) at midcell, with the remainder of
445 midcell iHT-aPBP1a or iHT-aPBP1a(S370A) molecules static (Fig. 5; Movie S19).
446 Essentially no circumferentially moving molecules of iHT-aPBP1a or iHT-
447 aPBP1a(S370A) were detected outside of midcell (Fig. 5). A similar conclusion was
448 reached when data from Figure 1*B* was sorted into midcell or non-midcell locations (Fig.
449 S20*A*). Since no PG synthesis was detectable by FDAA labeling away from the midcell
450 (Fig. 2 and S9), and nearly all aPBP1a molecules away from midcell were moving
451 diffusively (Fig. 5 and S20*A*), this further suggests that diffusively moving aPBP1a were
452 not actively synthesizing PG in exponentially growing cells. Taken together, these data
453 indicate that circumferentially moving iHT-aPBP1a molecules are actively synthesizing
454 PG, while inactive molecules are either static at midcell or moving diffusively throughout
455 the cell. A similar conclusion was reached for elongasome proteins iHT-bPBP2b, iHT-
456 RodA, and iHT-MreC (Fig. 1*B* and 2).

457 Other data were consistent with aPBP1a not being a constant component of the PG
458 elongasome. Notably, the velocity of iHT-aPBP1a in a merodiploid *iht-pbp1a*//P_{Zn}-*iht-*
459 *pbp1a* Δ*murZ* strain was similar to that of iHT-aPBP1a in a *murZ*$^+$ merodiploid strain (Fig.
460 S20*B*; Movie S20). Growth rate, protein amount, localization and relative frequency of
461 circumferential molecules of iHT-aPBP1a were also similar in the Δ*murZ* mutant and
462 *murZ*$^+$ strain (Fig. S19 and S20*C*). Therefore, unlike iHT-bPBP2b and iHT-RodA (Fig. 4*C*
463 and 4*D*), the circumferential velocity of iHT-aPBP1a was not decreased when PG

464 precursor amounts were reduced. In addition, we tested whether the relative frequency
465 of circumferential iHT-aPBP1a was changed in a *mpgA*(Y488D) Δ*pbp2b* mutant, which
466 lacks the core PG elongasome (80, 82). Reduced catalytic activity of MpgA(Y488D)
467 bypasses the requirement for the PG elongasome, but *mpgA*(Y488D) Δ*pbp2b* mutations
468 are synthetically lethal with Δ*pbp1a* (80), possibly indicating that aPBP1a can substitute
469 for the PG elongasome. Consistent with this notion, iHT-aPBP1a dynamics were the
470 same in a *mpgA*(Y488D) Δ*pbp2b* merodiploid strain as in a WT strain (Fig. S20*C*; Movie
471 S21).

472 **MpgA displays subdiffusive movement restricted to midcell.** We investigated the
473 dynamics of iHT-MpgA (previously MltG(*Spn*)) muramidase, which has been genetically
474 linked to elongasome PG synthesis (80, 82). At an image acquisition rate of 1 FPS, the
475 majority of iHT-MpgA molecules (≈87%) appeared to move diffusively, but seemed to be
476 constrained mainly to the midcell region of cells (Fig. 1*B*; Movie S22), consistent with a
477 previous report that sfGFP-MpgA localizes at midcell (34). The remaining ≈13% of iHT-
478 MpgA molecules were static at midcell (Fig. 1*B*). There was also a small fraction (<1%)
479 of iHT-MpgA molecules that appeared to display rapid (>50 nm/s) movement of very short
480 duration at midcell (Fig. 3*A*, 3*B*, and S21*A*). However, this motion was difficult to track
481 and at the limit of the criterion used for continuous motion (six consecutive frames).

482 Consequently, we increased the data acquisition rate to 10 FPS. At this higher rate,
483 iHT-MpgA did not exhibit the processive, unidirectional movement observed for the
484 elongasome components and for aPBP1a (Fig. 1*A* and S21*B*). Instead, iHT-MpgA moved
485 erratically, mainly in the midcell region (see below; Fig. S21*B*; Movie S23). Measured at
486 10 FPS, the mean velocity of iHT-MpgA moving in short, directional stretches was

487 relatively fast (≈327 nm/s) compared to circumferential movement of other proteins (<20
488 nm/s), but slower than diffusing molecules in non-midcell regions (>1,000 nm/s) (Fig.
489 S21*C*). These distinctive subdiffusive dynamics did not support persistent association of
490 MpgA with the PG elongasome or aPBP1a during PG synthesis.

491 Given these unusual dynamics, we confirmed the functionality of the iHT-MpgA fusion
492 construct. The growth and cell morphology of strains expressing iHT-MpgA were similar
493 to those of WT, and iHT-MpgA showed expected midcell localization (Fig. S2).
494 Additionally, full-length iHT-MpgA fusion protein was expressed at 171 ± 11% the amount
495 of WT MpgA, with only minimal degradation products observed (Fig. S6). A mutant
496 expressing partially active MpgA(Y488D) suppressed the essentiality of the
497 pneumococcal PG elongasome in transformation assays (80). However, the *iht-mpgA*
498 construct failed to suppress Δ*pbp2b*, Δ*rodA*, Δ*mreC*, or Δ*rodZ* in transformation assays
499 (Table S5), indicating iHT-MpgA possessed muramidase activity. Unlike Δ*mpgA* mutants,
500 which accumulate suppressor mutations that inactivate aPBP1a (80); no *pbp1a* mutations
501 were detected in the *iht-mpgA* fusion strain by Sanger DNA sequencing. These results
502 indicated that the iHT-MpgA fusion protein was substantially active and that its dynamics
503 accurately reflected those of WT MpgA.

504 **Core PG elongasome components and aPBP1a display different diffusion**
505 **patterns from MpgA.** We next investigated diffusion dynamics by performing sm-TIRFm
506 at 20 FPS (*Materials and Methods*). Individual molecular trajectories were tracked (Fig.
507 S22) and used to calculate mean-squared displacements (MSD) and diffusion coefficients
508 (Fig. 6) (106, 107). Diffusion coefficients were between 0.040 and 0.055 $\mu m^2/s$,
509 comparable to values determined previously for PG synthesis proteins in *S. pneumoniae*,

510 *E. coli* and *B. subtilis* (56, 100, 108, 109). Consistent with sm-TIRFm imaging at 1 FPS
511 (Fig. 1*B*), single molecules displayed rapid diffusive motion in non-midcell regions and
512 much slower, processive motion at midcell, where static molecules were also observed
513 (Fig. S22; Movies S24 to S30). MSD curves generated for diffusively moving molecules
514 were not linear and plateaued as time increased, with alpha values <1, which is indicative
515 of some form of subdiffusion (Fig. 6). Subdiffusion is commonly due to diffusion within a
516 confined space, but can also be caused by membrane crowding or interactions with other
517 molecules (110). For bacterial membrane proteins, this confined space is often the
518 surface area of the cell membrane (110).

519 Single-molecule trajectories of diffusively moving PG elongasome core components
520 iHT-bPBP2b, iHT-RodA, and iHT-MreC covered most of the cell area, while non-diffusive
521 processive and static molecules located to midcell, where active PG synthesis occurred
522 (Fig. S22; Movies S24 to S26), consistent with results acquired at 1 FPS (Fig. S8). This
523 suggests that the subdiffusive behavior of the core elongasome proteins was due to
524 confinement within the cell membrane. The diffusion coefficients of iHT-bPBP2b, iHT-
525 RodA, and iHT-MreC were similar (≈0.045 $\mu m^2/s$) and not statistically different (Fig. 6).
526 The MSD curves of diffusively moving iHT-bPBP2b, iHT-RodA, and iHT-MreC molecules
527 plateaued in the same range (≈0.075 μm^2), indicating that these core elongasome
528 components were confined to a similarly sized area (Fig. 6) (111).

529 Diffusively moving iHT-aPBP1a molecules appeared to have a slightly greater
530 diffusion coefficient (≈0.055 $\mu m^2/s$) compared to those of the core components of the PG
531 elongasome (Fig. 6); however, this apparent difference was not statistically significant.
532 iHT-aPBP1a molecules also appeared to have a higher plateau in MSD plots (≈0.1 μm^2)

533 (Fig. 6), consistent with diffusion over the whole cell (Fig. S22 and Movie S27); however,
534 again, this modest difference was not statistically different. Again, non-diffusive,
535 processively moving and static iHT-aPBP1a molecules were mostly confined to midcell
536 (Fig. S22), as was observed by sm-TIRFm at 1 FPS (Fig. 5 and S20*A*). Interestingly, we
537 also observed some diffusive iHT-aPBP1a molecules that stopped moving, paused for a
538 short time (<1 s), and then resumed diffusive movement (Movie S28). This pausing
539 behavior was not readily detectable for diffusing components of the PG elongasome. We
540 conclude that diffusing aPBP1a molecules move similarly to components of the core PG
541 elongasome in pneumococcal cells, but there is an intermediate paused state during
542 diffusion of aPBP1a.

543 Finally, diffusion analysis confirmed the unusual pattern of confined movement of iHT-
544 MpgA molecules at midcell. A substantial fraction of diffusing iHT-MpgA molecules
545 appeared to be confined to midcell, rather than over whole cells, like iHT-bPBP2b, iHT-
546 RodA, iHT-MreC, and iHT-aPBP1a (Fig. S22; Movie S29). This conclusion was
547 corroborated by manually counting the location of iHT-MpgA molecules from data (1 FPS)
548 in Figure 1*B*. This analysis showed that 58% (65/113) of subdiffusive iHT-MpgA
549 molecules were located within 125 nm of midcell septa or equatorial rings (Fig. S8, right).
550 By contrast, no diffusing iHT-MreC molecules were detected at midcell (Fig. S8). Confined
551 subdiffusion of iHT-MpgA is consistent with the low plateau (≈0.05 μm^2) in the MSD plot,
552 which was statistically different from those of iHT-bPBP2b, iHT-RodA, iHT-MreC, and
553 iHT-aPBP1a (Fig. 6). In addition, the diffusion coefficient (≈0.04 $\mu m^2/s$) of iHT-MpgA was
554 statistically lower than diffusing iHT-aPBP1a over the body of cells (Fig. 6), consistent
555 with the subdiffusive velocity of IHT-MpgA detected by sm-TIRFm at 10 FPS (Fig. S21C).

556 Similar to iHT-aPBP1a, iHT-MpgA subdiffusive molecules were observed transitioning
557 between diffusive motion and paused states (Movie S30). Together, these results indicate
558 that the confined, subdiffusive movement of MpgA molecules is fundamentally different
559 from that of components of the pneumococcal core PG elongasome and aPBP1a.
560

561 **DISCUSSION**

562 This paper shows that the core PG elongasome moves circumferentially around the
563 midcell of dividing *S. pneumoniae* cells (Fig. 1). The velocity of core elongasome
564 members bPBP2b, RodA, and MreC was statistically the same (≈11 nm/sec) (Fig. 3),
565 which is slightly slower than the velocity of the bPBP2x and FtsW (≈20 nm/sec)
566 components of the septal PG synthase (34). The processive motion of elongasome
567 members was driven by PG synthesis and was independent of FtsZ treadmilling (Fig. 4
568 and 5), and this motion was not dependent on stage of cell division (Fig. S10*B*). Strikingly,
569 the majority of bPBP2b or RodA molecules moved circumferentially in cells that severely
570 underproduced bPBP2b (≈15% of WT) or likely RodA (Fig. 1*B*). In contrast, in cells
571 expressing nearly WT protein levels, a minority of bPBP2b, RodA, and MreC molecules
572 either moved circumferentially and synthesized PG at midcell or exhibited nonmoving
573 static behavior at midcell (Fig. 1*B* and S8). The majority of core elongasome components
574 moved diffusively in the membrane over cell bodies, where PG synthesis was not
575 detected by FDAA labeling of exponentially growing cells (Fig. 2 and S9).

576 These observations indicate that pneumococcal elongation PG synthesis results from
577 processive, circumferential movement of PG elongasomes that are confined to a narrow
578 zone at midcell (Fig. 7 and S23). This pattern contrasts with the elongasome movement

579 guided by short MreB filaments and driven by PG synthesis that occurs over the body of
580 many rod-shaped bacteria (16). MreB-guided PG synthesis results in a dense mesh of
581 concentrically oriented PG glycan strands along the inner, sidewall surface of *B. subtilis*
582 cells (112). The circumferential movement of the pneumococcal PG elongasome
583 anticipates that peripheral PG glycan strands may likewise be concentrically aligned in *S.*
584 *pneumoniae* cells. These observations also indicate that in exponentially growing WT
585 cells, the core elongasome components are present in excess, with only a minority of
586 bPBP2b, RodA, and MreC engaged in active PG synthesis at midcell rings (Fig. 2 and
587 S9). In a new study of competence induction, processive, bidirectional movement of GFP-
588 bPBP2b and RodA-mNeonGreen at midcell was detected by ensemble-TIRFm in *S.*
589 *pneumoniae* laboratory strain R800 (113), which shows significant differences in shape
590 and the timing of cell division compared to the progenitor D39 strains used here (19, 33).
591 The velocities of bPBP2b or RodA were not changed by competence induction (113).

592 The results presented here further raise the issue of what directs circumferential
593 movement of elongasome components in tracks at midcell. The velocity of elongasome
594 components was not changed when treadmilling was greatly impeded in an *ftsZ*(GTPase)
595 mutant (Fig. 4*A*). Independence of FtsZ treadmilling fits the observation that FtsZ was not
596 detected in the outer midcell ring where peripheral PG synthesis occurs later in division
597 (Fig. S1*B*) (32). The similar velocity of MreC in predivisional cells when elongasomes are
598 still located in the FtsZ-ring as in later-divisional cells when the elongasome is in outer
599 midcell ring (Fig. S10*B*) is also consistent with independence of FtsZ treadmilling. In
600 addition, when RodA or bPBP2b was depleted, no unassociated bPBP2b or RodA was
601 detected being driven at the rate of treadmilling FtsZ (≈34 nm/sec; Fig. S17*D* and S17*E*),

602 as occurs for components of the septal PG synthase of *E. coli* (100). Moreover, a severe
603 decrease in FtsZ treadmilling speed led to only a marginal (≈17%) decrease in the speed
604 of the septal PG synthase in *S. pneumoniae* (34) and no decrease in *S. aureus* (55). In
605 *B. subtilis*, a slightly greater decrease (≈40%) in the speed of the septal PG synthase
606 when FtsZ treadmilling was moderately or greatly reduced has recently been attributed
607 to indirect effects (56). Thus, all evidence supports the conclusion that the movement and
608 speed of the septal and elongasome PG synthases in WT *S. pneumoniae* cells are driven
609 by PG synthesis, independent of FtsZ treadmilling.

610 It remains unknown what determines the tracks for the movement of the
611 pneumococcal septal or elongasome PG synthases in the inner and outer midcell rings,
612 respectively (Fig. S1). The muropeptide-crosslinked PG glycan strands to which new PG
613 is added may provide a rigid structure that directs processive PG synthesis in a linear
614 direction. Moreover, there appears to be a limited number of available sites in midcell
615 rings for septal and elongasome PG synthases to load and synthesize PG. As noted
616 above, only a minority of elongasome components are engaged in PG synthesis in WT
617 cells (Fig. 1*B*, 2, and S23). However, when the cellular amount of bPBP2b was reduced
618 to ≈15% of the WT level, the majority of bPBP2b molecules moved processively to
619 synthesize PG (Fig. 1*B*), consistent with a limited number of spots on rings for active PG
620 synthase complexes. Interestingly, ≈26% of circumferentially moving bPBP2b or MreC
621 molecules reversed direction within the timeframe of these experiments. Direction
622 reversal was also reported for processively moving members of the septal PG synthases
623 of *S. aureus* (55) and *B. subtilis* (114). This directional transitioning may be indicative of

624 PG synthase complexes stopping and reinitiating synthesis of a new glycan strand in the
625 opposite direction (55, 114).

626 We also observed nonmoving, static molecules of bPBP2b, RodA, and MreC
627 expressed at WT concentrations, primarily at midcell and to a lesser (≈5-fold) extent
628 elsewhere in cells (Fig. 1*B* and S8). When elongasome PG synthesis was halted by
629 expression of catalytically inactive proteins, circumferential movement also stopped and
630 molecules became static (Fig. 5, S13*C*, and S13*D*) (69). To our knowledge, there is no
631 direct evidence that PBPs static for several seconds are actively synthesizing PG, as
632 suggested for aPBPs in *E. coli* (71, 74). To the contrary, when PG synthases stop
633 synthesis, they stop moving (Fig. 5, S13*C*, and S13*D*) (34, 55, 56, 115). Therefore, we
634 think it more likely that static PG synthases at midcell in WT cells may be incompletely
635 assembled complexes or complexes waiting to assume an available site for PG synthesis,
636 possibly stabilized by noncovalent binding of PBP TP domains to acceptor peptides in
637 PG (56, 109). Consistent with this idea, we observed transitions of MreC molecules from
638 the processive to static states (<5%), and *vice versa* (<1%). The mechanisms that
639 arrange and limit the number of active pneumococcal PG elongasomes remain to be
640 determined.

641 The processive movement of pneumococcal Class A aPBP1a strikingly contrasts with
642 the diffusive motion for Class A PBPs reported previously in *E. coli* and *B. subtilis* (71,
643 74). Earlier IFM studies colocalized aPBP1a with elongasome components bPBP2b and
644 MreC (35). Instead of diffusive motion, aPBP1a molecules at midcell moved
645 circumferentially or were static (Fig. 5 and S20), and processive movement was abolished
646 in a *pbp1a*(TP) mutant (Fig. 5). Processively moving aPBP1a also reversed direction

647 infrequently (<9%). However, several results indicate that aPBP1a is not a persistent
648 member of the core PG elongasome. The duration of aPBP1a processive motion was
649 considerably shorter (≈10 s) than that of the PG elongasome components (≈23 s) (Fig.
650 3*B*). In addition, the relative frequency of circumferential motion of aPBP1a was
651 unchanged in a suppressed Δ*pbp2b mpgA*(Y488D) mutant that lacks an intact PG
652 elongasome (Fig. S20*C*). Like iHT-bPBP2b, iHT-aPBP1a was underproduced (10% of
653 WT) when expressed from its native chromosomal locus (Fig. 1*B* and S5*B*). But, unlike
654 iHT-bPBP2b, circumferentially moving aPBP1a was not the majority species at the low
655 expression level (Fig. 1*B*). In addition, unlike bPBP2b and RodA, aPBP1a processive
656 motion was not decreased in a Δ*murZ* mutant (Fig. S20*B* and S20*C*), which may reflect
657 a different kinetic dependence for Lipid II substrate. Outside of midcell, aPBP1a moved
658 diffusively in the membrane over the whole length of cells (Fig. 5 and S22). Together,
659 these results indicate that aPBP1a is not a persistent member of the pneumococcal core
660 PG elongasome (85), although shorter or transient interactions are possible (Fig. 7).

661 aPBPs have been proposed to play roles in normal PG synthesis and in repair of
662 damaged PG (1, 39, 73, 116). In rod-shaped bacteria, it was postulated that when
663 diffusing aPBPs encounter damaged PG, they cease moving and become static for
664 relatively long times (≈5 s) (71, 74). For reasons discussed above, long static PG
665 synthases may not be synthesizing PG. We also detected another aPBP1a motion away
666 from midcell in exponentially growing cells. Diffusing aPBP1a molecules infrequently
667 paused for short (<1 s) intervals, before resuming diffusive motion (Movie S28). It remains
668 to be determined whether static or paused aPBP1a molecules are repairing damaged PG
669 in *S. pneumoniae* cells.

670 In Gram-positive bacteria, the PG in the septal annular disk has a core of concentric
671 ordered PG glycan strands covered by a dense mesh of randomly oriented PG strands
672 that face the cell membrane (112). It has been postulated that aPBPs may synthesize this
673 layer of randomly oriented, inner-facing PG strands (39), although remodeling by PG
674 hydrolases followed by resynthesis could potentially contribute to this disordered pattern.
675 Circumferential, processive movement suggests that aPBP1a synthesis may result in
676 concentric, ordered PG glycan strands, rather than randomly oriented strands. Glycan
677 strands synthesized by the shorter tracks of aPBP1a motion are presumably shorter than
678 those synthesized by the more processive core PG elongasome. These shorter strands
679 may be remodeled and crosslinked into the longer strands to provide additional strength
680 to the peripheral PG layer. The dynamics of the other pneumococcal Class A PBPs,
681 aPBP2a and aPBP1b, remains to be determined. The circumferential movement of an
682 aPBP potentially has another implication to bacteria that elongate only from their poles,
683 such as *Rhizobiales* species, including *Agrobacterium tumefaciens* (117, 118). Polar
684 elongasome complexes in these bacteria lack bPBP:SEDS PG synthases, and PG
685 elongation is carried out only by a single essential aPBP (117, 118), which may move
686 circumferentially during PG elongation.

687 Finally, the subdiffusional, confined motion of the MpgA muramidase at midcell was
688 unexpected. IFM showed that MpgA (formerly MltG(*Spn*)), like aPBP1a, colocalized with
689 MreC to the outer ring in later-divisional cells (80). MpgA is an essential muramidase that
690 cleaves newly synthesized PG glycan chains 7 disaccharides from the undecaprenol
691 membrane anchor (82). A LysM domain in MpgA correctly places the cleavage point in
692 the glycan chain. Therefore, MpgA is thought to act as a PG release factor that frees

693 newly synthesized PG for crosslinking into existing PG (82). Instead of moving
694 circumferentially, most MpgA molecules moved at subdiffusion speeds (≈300 nm/sec)
695 that were slower than that of freely diffusing MpgA (>1,000 nm/sec). However, instead of
696 moving over the whole body of cells, most MpgA molecules were confined to regions of
697 PG synthesis at midcell (Fig. 1*B*, S*8*, and S22). Therefore, MpgA functions separately
698 from the core PG elongasome and from aPBP1a (Fig. 7). Only a fraction (≈15%) of MpgA
699 molecules were static, mostly at midcell (Fig. 1*B* and S*8*), and we detected subdiffusing
700 MpgA molecules that paused (<1 s) and then resumed movement (Movie S30), similar to
701 aPBP1a. Whether static or paused MpgA are carrying out PG strand cleavage requires
702 further study. Likewise, proteins that interact with and regulate MpgA activity (119) and
703 the mechanism that confines MpgA movement to midcell await discovery.
704

705 **MATERIALS AND METHODS**

706 Bacterial strains used were unencapsulated (Δ*cps*) derivatives of *Streptococcus*
707 *pneumoniae* (*Spn*) serotype 2 strain D39W and are listed in Table S1. IU1945 and IU1824
708 were used as parent strains (Table S1). Detailed methods are described in *Supplemental*
709 *Materials and Methods*, including: bacterial strain construction and growth conditions;
710 ectopic expression and depletion conditions; cell labeling with HaloTag ligand; 2D-
711 epifluorescence microscopy and analysis; sm-TIRFm sample preparation; sm-TIRFm
712 imaging; sm-TIRFm image analysis; single-molecule tracking and diffusion analysis; 3D-
713 structured illumination microscopy and analysis; quantitative western blotting;
714 transformation assay.
715

716 **ACKNOWLEDGEMENTS**

717 We thank laboratory members and Jie Xiao (Johns Hopkins) for discussions about this
718 work; John D. Richardson and Ziyun A. Ye for technical assistance with some
719 experiments, Jim Powers (Indiana University Bloomington) for advice about light
720 microscopy; Mike VanNieuwenhze (Indiana University Bloomington) for FDAA reagents;
721 Luke Lavis (Janelia Lab) for Fluor JF549; Reinhold Brückner, and Regine Hakenbeck
722 (Kaiserlautern University) for anti-bPBP2x antibody; and Suzanne Walker and David Z.
723 Rudner (Harvard Medical School) for antibodies against pneumococcal PG synthesis
724 proteins. This work was supported by NIH brant R35GM131767 (to MEW), NSF grant
725 MCB1027504 (to SLS); NIH grant RO1AI148752 (to Suzanne Walker); NIH grant T32
726 GM109825 (to AJP); NIH grant F31AI138430 (to MML); NIH grants T32 GM007753 and
727 F30 AI156972 (to JEP), and NIH equipment grant S10OD024988 to the Indiana University
728 Bloomington (IUB) Light Microscopy Imaging Center.

729

730 **CONFLICT OF INTEREST**

731 The authors declare that they have no conflicts of interests.

732

733 **AUTHOR CONTRIBUTIONS**

734 AJP, MML, KEB, SLS, and MEW contributed to the conception or design of this study.
735 AJP, MML, KEB, MAT, JEP SLS, HCTT, and MEW contributed to the acquisition,
736 analysis, and interpretation of the data. KEB, HCTT, and MEW contributed to the writing
737 of the manuscript with input from the other authors.

738

DATA AVAILABILITY

The data that support the findings of this study are presented in the paper, including the Supplemental Information and Dataset S1.

ORCID

Amilcar J. Perez https://orcid.org/0000-0001-6729-7564

Melissa M. Lamanna https://orcid.org/0000-0002-6535-7903

Kevin E. Bruce https://orcid.org/0009-0005-3300-8863

Marc A. Touraev https://orcid.org/0000-0001-8351-6413

Julia E. Page https://orcid.org/0000-0002-9884-2382

Sidney L. Shaw https://orcid.org/0000-0001-9195-6128

Ho-Ching T. Tsui https://orcid.org/0000-0003-0849-874X

Malcolm E. Winkler https://orcid.org/0000-0002-1482-2588

REFERENCES

1. E. A. Mueller, P. A. Levin, Bacterial Cell Wall Quality Control during Environmental Stress. *mBio* **11** 10.1128/mBio.02456-20 (2020).
2. M. Rajagopal, S. Walker, Envelope Structures of Gram-Positive Bacteria. *Curr Top Microbiol Immunol* **404**, 1-44 (2017).
3. E. R. Rojas, The Mechanical Properties of Bacteria and Why they Matter. *Adv Exp Med Biol* **1267**, 1-14 (2020).
4. W. Vollmer, O. Massidda, A. Tomasz, The Cell Wall of Streptococcus pneumoniae. *Microbiol Spectr* **7** 10.1128/microbiolspec.GPP3-0018-2018 (2019).
5. K. D. Young, Bacterial shape: two-dimensional questions and possibilities. *Annu Rev Microbiol* **64**, 223-240 (2010).
6. K. Bush, P. A. Bradford, Interplay between beta-lactamases and new beta-lactamase inhibitors. *Nat Rev Microbiol* **17**, 295-306 (2019).
7. T. den Blaauwen, J. M. Andreu, O. Monasterio, Bacterial cell division proteins as antibiotic targets. *Bioorg Chem* **55**, 27-38 (2014).
8. K. Lewis, The Science of Antibiotic Discovery. *Cell* **181**, 29-45 (2020).

9. L. L. Ling *et al.*, A new antibiotic kills pathogens without detectable resistance. *Nature* **517**, 455-459 (2015).
10. L. T. Sham, H. C. Tsui, A. D. Land, S. M. Barendt, M. E. Winkler, Recent advances in pneumococcal peptidoglycan biosynthesis suggest new vaccine and antimicrobial targets. *Curr Opin Microbiol* **15**, 194-203 (2012).
11. J. Zhou *et al.*, Breaking down the cell wall: Still an attractive antibacterial strategy. *Front Microbiol* **13**, 952633 (2022).
12. S. Booth, R. J. Lewis, Structural basis for the coordination of cell division with the synthesis of the bacterial cell envelope. *Protein Sci* **28**, 2042-2054 (2019).
13. A. J. F. Egan, J. Errington, W. Vollmer, Regulation of peptidoglycan synthesis and remodelling. *Nat Rev Microbiol* **18**, 446-460 (2020).
14. S. Garde, P. K. Chodisetti, M. Reddy, Peptidoglycan: Structure, Synthesis, and Regulation. *EcoSal Plus* **9** 10.1128/ecosalplus.ESP-0010-2020 (2021).
15. S. Kumar, A. Mollo, D. Kahne, N. Ruiz, The Bacterial Cell Wall: From Lipid II Flipping to Polymerization. *Chem Rev* **122**, 8884-8910 (2022).
16. P. D. A. Rohs, T. G. Bernhardt, Growth and Division of the Peptidoglycan Matrix. *Annu Rev Microbiol* **75**, 315-336 (2021).
17. C. Billaudeau *et al.*, Contrasting mechanisms of growth in two model rod-shaped bacteria. *Nat Commun* **8**, 15370 (2017).
18. P. J. Eswara, K. S. Ramamurthi, Bacterial Cell Division: Nonmodels Poised to Take the Spotlight. *Annu Rev Microbiol* **71**, 393-411 (2017).
19. M. M. Lamanna *et al.*, Roles of RodZ and class A PBP1b in the assembly and regulation of the peripheral peptidoglycan elongasome in ovoid-shaped cells of Streptococcus pneumoniae D39. *Mol Microbiol* **118**, 336-368 (2022).
20. S. P. Ouellette, J. Lee, J. V. Cox, Division without Binary Fission: Cell Division in the FtsZ-Less Chlamydia. *J Bacteriol* **202** 10.1128/JB.00252-20 (2020).
21. A. R. Pereira *et al.*, FtsZ-Dependent Elongation of a Coccoid Bacterium. *mBio* **7** 10.1128/mBio.00908-16 (2016).
22. M. G. Pinho, M. Kjos, J. W. Veening, How to get (a)round: mechanisms controlling growth and division of coccoid bacteria. *Nat Rev Microbiol* **11**, 601-614 (2013).
23. A. M. Randich, Y. V. Brun, Molecular mechanisms for the evolution of bacterial morphologies and growth modes. *Front Microbiol* **6**, 580 (2015).
24. N. S. Briggs, K. E. Bruce, S. Naskar, M. E. Winkler, D. I. Roper, The Pneumococcal Divisome: Dynamic Control of Streptococcus pneumoniae Cell Division. *Front Microbiol* **12**, 737396 (2021).
25. O. Massidda, L. Novakova, W. Vollmer, From models to pathogens: how much have we learned about Streptococcus pneumoniae cell division? *Environ Microbiol* **15**, 3133-3157 (2013).
26. M. J. Cox, N. Loman, D. Bogaert, J. O'Grady, Co-infections: potentially lethal and unexplored in COVID-19. *Lancet Microbe* **1**, e11 (2020).
27. V. Sender, K. Hentrich, B. Henriques-Normark, Virus-Induced Changes of the Respiratory Tract Environment Promote Secondary Infections With Streptococcus pneumoniae. *Front Cell Infect Microbiol* **11**, 643326 (2021).
28. J. N. Weiser, D. M. Ferreira, J. C. Paton, Streptococcus pneumoniae: transmission, colonization and invasion. *Nat Rev Microbiol* **16**, 355-367 (2018).

29. CDC (2019) Antibiotic resistance threats in the United States, 2019. in *AR Threats Rep., U.S. Dep. Health Hum. Serv., Cent. Dis. Control Prev.* (AR Threats Report, U.S.A. Dept Health and Human Services, Center for Disease Control and Prevention, Atlanta, GA).
30. P. S. Gibson, J. W. Veening, Gaps in the wall: understanding cell wall biology to tackle amoxicillin resistance in Streptococcus pneumoniae. *Curr Opin Microbiol* **72**, 102261 (2023).
31. WHO (2017) List of bacteria for which new antibiotics are urgently needed. (World Health Organization, Geneva, Switzerland).
32. A. J. Perez *et al.*, Organization of peptidoglycan synthesis in nodes and separate rings at different stages of cell division of Streptococcus pneumoniae. *Mol Microbiol* **115**, 1152-1169 (2021).
33. J. Trouve *et al.*, Nanoscale dynamics of peptidoglycan assembly during the cell cycle of Streptococcus pneumoniae. *Curr Biol* **31**, 2844-2856 e2846 (2021).
34. A. J. Perez *et al.*, Movement dynamics of divisome proteins and PBP2x:FtsW in cells of Streptococcus pneumoniae. *Proc Natl Acad Sci U S A* **116**, 3211-3220 (2019).
35. H. T. Tsui *et al.*, Pbp2x localizes separately from Pbp2b and other peptidoglycan synthesis proteins during later stages of cell division of Streptococcus pneumoniae D39. *Mol Microbiol* **94**, 21-40 (2014).
36. J. Errington, L. J. Wu, Cell Cycle Machinery in Bacillus subtilis. *Subcell Biochem* **84**, 67-101 (2017).
37. V. A. Lund *et al.*, Molecular coordination of Staphylococcus aureus cell division. *Elife* **7** 10.7554/eLife.32057 (2018).
38. B. M. Saraiva *et al.*, Reassessment of the distinctive geometry of Staphylococcus aureus cell division. *Nat Commun* **11**, 4097 (2020).
39. D. Straume, K. W. Piechowiak, M. Kjos, L. S. Havarstein, Class A PBPs: It is time to rethink traditional paradigms. *Mol Microbiol* **116**, 41-52 (2021).
40. R. Wheeler, S. Mesnage, I. G. Boneca, J. K. Hobbs, S. J. Foster, Super-resolution microscopy reveals cell wall dynamics and peptidoglycan architecture in ovococcal bacteria. *Mol Microbiol* **82**, 1096-1109 (2011).
41. A. J. Perez *et al.*, FtsZ-Ring Regulation and Cell Division Are Mediated by Essential EzrA and Accessory Proteins ZapA and ZapJ in Streptococcus pneumoniae. *Front Microbiol* **12**, 780864 (2021).
42. A. Fleurie *et al.*, MapZ marks the division sites and positions FtsZ rings in Streptococcus pneumoniae. *Nature* **516**, 259-262 (2014).
43. N. Holeckova *et al.*, LocZ is a new cell division protein involved in proper septum placement in Streptococcus pneumoniae. *mBio* **6**, e01700-01714 (2014).
44. V. W. Rowlett, W. Margolin, The Min system and other nucleoid-independent regulators of Z ring positioning. *Front Microbiol* **6**, 478 (2015).
45. L. J. Wu, J. Errington, Nucleoid occlusion and bacterial cell division. *Nat Rev Microbiol* **10**, 8-12 (2011).
46. A. D. Land *et al.*, Requirement of essential Pbp2x and GpsB for septal ring closure in Streptococcus pneumoniae D39. *Mol Microbiol* **90**, 939-955 (2013).

858 47. R. van Raaphorst, M. Kjos, J. W. Veening, Chromosome segregation drives
859 division site selection in Streptococcus pneumoniae. *Proc Natl Acad Sci U S A*
860 **114**, E5959-E5968 (2017).
861 48. M. Jacq *et al.*, Remodeling of the Z-Ring Nanostructure during the Streptococcus
862 pneumoniae Cell Cycle Revealed by Photoactivated Localization Microscopy.
863 *mBio* **6** 10.1128/mBio.01108-15 (2015).
864 49. A. Mura *et al.*, Roles of the Essential Protein FtsA in Cell Growth and Division in
865 Streptococcus pneumoniae. *J Bacteriol* **199** 10.1128/JB.00608-16 (2017).
866 50. P. A. Levin, A. Janakiraman, Localization, Assembly, and Activation of the
867 Escherichia coli Cell Division Machinery. *EcoSal Plus* **9**, eESP00222021 (2021).
868 51. C. R. Mahone, E. D. Goley, Bacterial cell division at a glance. *J Cell Sci* **133** (2020).
869 52. L. M. Y. Mertens, T. den Blaauwen, Optimising expression of the large dynamic
870 range FRET pair mNeonGreen and superfolder mTurquoise2(ox) for use in the
871 Escherichia coli cytoplasm. *Sci Rep* **12**, 17977 (2022).
872 53. A. W. Bisson-Filho *et al.*, Treadmilling by FtsZ filaments drives peptidoglycan
873 synthesis and bacterial cell division. *Science* **355**, 739-743 (2017).
874 54. X. Yang *et al.*, A two-track model for the spatiotemporal coordination of bacterial
875 septal cell wall synthesis revealed by single-molecule imaging of FtsW. *Nat*
876 *Microbiol* **6**, 584-593 (2021).
877 55. S. Schäper *et al.*, Cell constriction requires processive septal peptidoglycan
878 synthase movement indpendent of FtsZ treadmilling in *Staphylococcus aureus*.
879 *Nat Microbiol* **9**: 1049-1063 (2024).
880 56. K. D. Whitley, J. Grimshaw, D. M. Roberts, E. Karinou, P. J. Stansfeld, S. Holden,
881 Peptidoglycan synthesis drives a single population of septal synthases during
882 division of *Bacillus subtilis*. *Nat Microbiol* **9**: 1064-1074 (2024).
883 57. J. Dominguez-Escobar *et al.*, Processive movement of MreB-associated cell wall
884 biosynthetic complexes in bacteria. *Science* **333**, 225-228 (2011).
885 58. E. C. Garner *et al.*, Coupled, circumferential motions of the cell wall synthesis
886 machinery and MreB filaments in B. subtilis. *Science* **333**, 222-225 (2011).
887 59. S. van Teeffelen *et al.*, The bacterial actin MreB rotates, and rotation depends on
888 cell-wall assembly. *Proc Natl Acad Sci U S A* **108**, 15822-15827 (2011).
889 60. B. P. Bratton, J. W. Shaevitz, Z. Gitai, R. M. Morgenstein, MreB polymers and
890 curvature localization are enhanced by RodZ and predict E. coli's cylindrical
891 uniformity. *Nat Commun* **9**, 2797 (2018).
892 61. S. Hussain *et al.*, MreB filaments align along greatest principal membrane
893 curvature to orient cell wall synthesis. *Elife* **7**, e32471 (2018).
894 62. R. M. Morgenstein *et al.*, RodZ links MreB to cell wall synthesis to mediate MreB
895 rotation and robust morphogenesis. *Proc Natl Acad Sci U S A* **112**, 12510-12515
896 (2015).
897 63. R. Ago, D. Shiomi, RodZ: a key-player in cell elongation and cell division in
898 Escherichia coli. *AIMS Microbiol* **5**, 358-367 (2019).
899 64. F. O. Bendezu, C. A. Hale, T. G. Bernhardt, P. A. de Boer, RodZ (YfgA) is required
900 for proper assembly of the MreB actin cytoskeleton and cell shape in E. coli. *EMBO*
901 *J* **28**, 193-204 (2009).

902 65. F. van den Ent, C. M. Johnson, L. Persons, P. de Boer, J. Lowe, Bacterial actin
903 MreB assembles in complex with cell shape protein RodZ. *EMBO J* **29**, 1081-1090
904 (2010).
905 66. A. J. Meeske *et al.*, SEDS proteins are a widespread family of bacterial cell wall
906 polymerases. *Nature* **537**, 634-638 (2016).
907 67. P. D. A. Rohs *et al.*, A central role for PBP2 in the activation of peptidoglycan
908 polymerization by the bacterial cell elongation machinery. *PLoS Genet* **14**,
909 e1007726 (2018).
910 68. P. D. A. Rohs *et al.*, Identification of potential regulatory domains within the MreC
911 and MreD components of the cell elongation machinery. *J Bacteriol*
912 10.1128/JB.00493-20 (2021).
913 69. M. Sjodt *et al.*, Structure of the peptidoglycan polymerase RodA resolved by
914 evolutionary coupling analysis. *Nature* **556**, 118-121 (2018).
915 70. M. Sjodt *et al.*, Structural coordination of polymerization and crosslinking by a
916 SEDS-bPBP peptidoglycan synthase complex. *Nat Microbiol* **5**, 813-820 (2020).
917 71. H. Cho *et al.*, Bacterial cell wall biogenesis is mediated by SEDS and PBP
918 polymerase families functioning semi-autonomously. *Nat Microbiol* **1**, 16172
919 (2016).
920 72. M. F. Dion *et al.*, Bacillus subtilis cell diameter is determined by the opposing
921 actions of two distinct cell wall synthetic systems. *Nat Microbiol* **4**, 1294-1305
922 (2019).
923 73. M. Pazos, W. Vollmer, Regulation and function of class A Penicillin-binding
924 proteins. *Curr Opin Microbiol* **60**, 80-87 (2021).
925 74. A. Vigouroux *et al.*, Class-A penicillin binding proteins do not contribute to cell
926 shape but repair cell-wall defects. *Elife* **9**, e51998 (2020).
927 75. K. H. Berg, G. A. Stamsas, D. Straume, L. S. Havarstein, Effects of low PBP2b
928 levels on cell morphology and peptidoglycan composition in Streptococcus
929 pneumoniae R6. *J Bacteriol* **195**, 4342-4354 (2013).
930 76. J. Philippe, T. Vernet, A. Zapun, The elongation of ovococci. *Microb Drug Resist*
931 **20**, 215-221 (2014).
932 77. G. A. Stamsas *et al.*, Identification of EloR (Spr1851) as a regulator of cell
933 elongation in Streptococcus pneumoniae. *Mol Microbiol* **105**, 954-967 (2017).
934 78. D. Straume, G. A. Stamsas, K. H. Berg, Z. Salehian, L. S. Havarstein, Identification
935 of pneumococcal proteins that are functionally linked to penicillin-binding protein
936 2b (PBP2b). *Mol Microbiol* **103**, 99-116 (2017).
937 79. J. J. Zheng, A. J. Perez, H. T. Tsui, O. Massidda, M. E. Winkler, Absence of the
938 KhpA and KhpB (JAG/EloR) RNA-binding proteins suppresses the requirement for
939 PBP2b by overproduction of FtsA in Streptococcus pneumoniae D39. *Mol*
940 *Microbiol* **106**, 793-814 (2017).
941 80. H. C. Tsui *et al.*, Suppression of a deletion mutation in the gene encoding essential
942 PBP2b reveals a new lytic transglycosylase involved in peripheral peptidoglycan
943 synthesis in Streptococcus pneumoniae D39. *Mol Microbiol* **100**, 1039-1065
944 (2016).
945 81. A. D. Land, M. E. Winkler, The requirement for pneumococcal MreC and MreD is
946 relieved by inactivation of the gene encoding PBP1a. *J Bacteriol* **193**, 4166-4179
947 (2011).

948 82. A. Taguchi, J. E. Page, H. T. Tsui, M. E. Winkler, S. Walker, Biochemical
949 reconstitution defines new functions for membrane-bound glycosidases in
950 assembly of the bacterial cell wall. *Proc Natl Acad Sci U S A* **118**
951 10.1073/pnas.2103740118 (2021).
952 83. A. K. Fenton, L. El Mortaji, D. T. Lau, D. Z. Rudner, T. G. Bernhardt, CozE is a
953 member of the MreCD complex that directs cell elongation in Streptococcus
954 pneumoniae. *Nat Microbiol* **2**, 16237 (2016).
955 84. M. M. Lamanna, A. T. Maurelli, What Is Motion? Recent Advances in the Study of
956 Molecular Movement Patterns of the Peptidoglycan Synthesis Machines. *J*
957 *Bacteriol* **204**, e0059821 (2022).
958 85. C. Lenoir *et al.*, The morphogenic protein CopD controls the spatio-temporal
959 dynamics of PBP1a and PBP2b in Streptococcus pneumoniae. *mBio* **14**,
960 e0141123 (2023).
961 86. S. G. Bartual *et al.*, Structural basis of PcsB-mediated cell separation in
962 Streptococcus pneumoniae. *Nature communications* **5**, 3842 (2014).
963 87. B. E. Rued *et al.*, Structure of the Large Extracellular Loop of FtsX and Its
964 Interaction with the Essential Peptidoglycan Hydrolase PcsB in Streptococcus
965 pneumoniae. *mBio* **10** 10.1128/mBio.02622-18 (2019).
966 88. L. T. Sham, S. M. Barendt, K. E. Kopecky, M. E. Winkler, Essential PcsB putative
967 peptidoglycan hydrolase interacts with the essential FtsXSpn cell division protein
968 in Streptococcus pneumoniae D39. *Proc Natl Acad Sci U S A* **108**, E1061-1069
969 (2011).
970 89. L. T. Sham, K. R. Jensen, K. E. Bruce, M. E. Winkler, Involvement of FtsE ATPase
971 and FtsX extracellular loops 1 and 2 in FtsEX-PcsB complex function in cell
972 division of Streptococcus pneumoniae D39. *mBio* **4** 10.1128/mBio.00431-13
973 (2013).
974 90. P. Domínguez-Cuevas, I. Porcelli, R. A. Daniel, J. Errington, Differentiated roles
975 for MreB-actin isologues and autolytic enzymes in Bacillus subtilis morphogenesis.
976 *Mol Microbiol* **89**, 1084-1098 (2013).
977 91. J. Meisner *et al.*, FtsEX is required for CwlO peptidoglycan hydrolase activity
978 during cell wall elongation in Bacillus subtilis. *Mol Microbiol* **89**, 1069-1083 (2013).
979 92. M. J. Catalão, J. Figueiredo, M. X. Henriques, J. P. Gomes, S. R. Filipe,
980 Optimization of fluorescent tools for cell biology studies in Gram-positive bacteria.
981 *PLoS One* **9**, e113796 (2014).
982 93. J. B. Grimm *et al.*, A general method to improve fluorophores for live-cell and
983 single-molecule microscopy. *Nat Methods* **12**, 244-250, 243 p following 250
984 (2015).
985 94. M. X. Henriques, M. J. Catalão, J. Figueiredo, J. P. Gomes, S. R. Filipe,
986 Construction of improved tools for protein localization studies in Streptococcus
987 pneumoniae. *PLoS One* **8**, e55049 (2013).
988 95. G. V. Los *et al.*, HaloTag: a novel protein labeling technology for cell imaging and
989 protein analysis. *ACS Chem Biol* **3**, 373-382 (2008).
990 96. K. Peters *et al.*, Streptococcus pneumoniae PBP2x mid-cell localization requires
991 the C-terminal PASTA domains and is essential for cell shape maintenance. *Mol*
992 *Microbiol* **92**, 733-755 (2014).

97. N. Ke, D. Landgraf, J. Paulsson, M. Berkmen, Visualization of Periplasmic and Cytoplasmic Proteins with a Self-Labeling Protein Tag. *J Bacteriol* **198**, 1035-1043 (2016).
98. A. Eberhardt, L. J. Wu, J. Errington, W. Vollmer, J. W. Veening, Cellular localization of choline-utilization proteins in Streptococcus pneumoniae using novel fluorescent reporter systems. *Mol Microbiol* **74**, 395-408 (2009).
99. F. E. Jacobsen, K. M. Kazmierczak, J. P. Lisher, M. E. Winkler, D. P. Giedroc, Interplay between manganese and zinc homeostasis in the human pathogen Streptococcus pneumoniae. *Metallomics : Integrated Biometal Science* **3**, 38-41 (2011).
100. J. W. McCausland *et al.*, Treadmilling FtsZ polymers drive the directional movement of sPG-synthesis enzymes via a Brownian ratchet mechanism. *Nat Commun* **12**, 609 (2021).
101. H. T. Tsui *et al.*, Negative regulation of MurZ and MurA underlies the essentiality of GpsB- and StkP-mediated protein phosphorylation in Streptococcus pneumoniae D39. *Mol Microbiol* **120**, 351-383 (2023).
102. O. Kocaoglu, H. C. Tsui, M. E. Winkler, E. E. Carlson, Profiling of β-lactam selectivity for penicillin-binding proteins in Streptococcus pneumoniae D39. *Antimicrob Agents Chemother* **59**, 3548-3555 (2015).
103. K. H. Berg, D. Straume, L. S. Havarstein, The function of the transmembrane and cytoplasmic domains of pneumococcal penicillin-binding proteins 2x and 2b extends beyond that of simple anchoring devices. *Microbiology (Reading)* **160**, 1585-1598 (2014).
104. H. Cho, T. Uehara, T. G. Bernhardt, Beta-lactam antibiotics induce a lethal malfunctioning of the bacterial cell wall synthesis machinery. *Cell* **159**, 1300-1311 (2014).
105. I. Shlosman *et al.*, Allosteric activation of cell wall synthesis during bacterial growth. *Nat Commun* **14**, 3439 (2023).
106. N. Tarantino *et al.*, TNF and IL-1 exhibit distinct ubiquitin requirements for inducing NEMO-IKK supramolecular structures. *J Cell Biol* **204**, 231-245 (2014).
107. J. Y. Tinevez *et al.*, TrackMate: An open and extensible platform for single-particle tracking. *Methods* **115**, 80-90 (2017).
108. T. K. Lee *et al.*, A dynamically assembled cell wall synthesis machinery buffers cell growth. *Proc Natl Acad Sci U S A* **111**, 4554-4559 (2014).
109. G. Ozbaykal *et al.*, The transpeptidase PBP2 governs initial localization and activity of the major cell-wall synthesis machinery in E. coli. *Elife* **9** 10.7554/eLife.50629 (2020).
110. C. H. Bohrer, J. Xiao, Complex Diffusion in Bacteria. *Adv Exp Med Biol* **1267**, 15-43 (2020).
111. A. Kusumi, Y. Sako, M. Yamamoto, Confined lateral diffusion of membrane receptors as studied by single particle tracking (nanovid microscopy). Effects of calcium-induced differentiation in cultured epithelial cells. *Biophys J* **65**, 2021-2040 (1993).
112. L. Pasquina-Lemonche *et al.*, The architecture of the Gram-positive bacterial cell wall. *Nature* **582**, 294-297 (2020).

1038 113. D. Juillot *et al.*, Transient inhibition of cell division in competent pneumococcal cells
1039 results from deceleration of the septal peptidoglycan complex. *bioRxiv*
1040 10.1101/2024.02.28.582556 (2024).
1041 114. S. Middlemiss *et al.*, Molecular motor tug-of-war regulates elongasome cell wall
1042 synthesis dynamics in Bacillus subtilis. *bioRxiv* 10.1101/2023.05.10.540107,
1043 2023.2005.2010.540107 (2023).
1044 115. Z. Lyu *et al.*, FtsN maintains active septal cell wall synthesis by forming a
1045 processive complex with the septum-specific peptidoglycan synthases in E. coli.
1046 *Nat Commun* **13**, 5751 (2022).
1047 116. D. Straume *et al.*, Class A PBPs have a distinct and unique role in the construction
1048 of the pneumococcal cell wall. *Proc Natl Acad Sci U S A* **117**, 6129-6138 (2020).
1049 117. W. M. Figueroa-Cuilan, P. J. B. Brown, Cell Wall Biogenesis During Elongation
1050 and Division in the Plant Pathogen Agrobacterium tumefaciens. *Curr Top Microbiol*
1051 *Immunol* **418**, 87-110 (2018).
1052 118. M. A. Williams *et al.*, Unipolar Peptidoglycan Synthesis in the Rhizobiales Requires
1053 an Essential Class A Penicillin-Binding Protein. *mBio* **12**, e0234621 (2021).
1054 119. A. R. Winther, M. Kjos, M. L. Herigstad, L. S. Havarstein, D. Straume, EloR
1055 interacts with the lytic transglycosylase MltG at midcell in Streptococcus
1056 pneumoniae R6. *J Bacteriol* 10.1128/JB.00691-20 (2021).

1057

1058 **FIGURE LEGENDS**

1059 **Fig. 1.** Elongation PG synthesis proteins displayed processive circumferential motion,
1060 and a limited number of molecules simultaneously engaged in PG synthesis. Sm-TIRFm
1061 was performed at 1 FPS as described in *Materials and Methods* on strains *iht-pbp2b*
1062 (IU15928), *iht-pbp2b* // P_{Zn}-*iht-pbp2b* (IU16553), *iht-rodA* (IU15970), *iht-rodA* // P_{Zn}-*iht-*
1063 *rodA* (IU16496), *iht-mreC* (IU16344), *iht-pbp1a* (IU16320), *iht-pbp1a* // P_{Zn}-*iht-pbp1a*
1064 (IU16497), and *iht-mpgA* (IU15997). (*A*) Representative time-lapse images and
1065 kymographs of molecules displaying processive circumferential movement in strains
1066 IU15928, IU15970, IU16344, and IU16497. Cell outlines are DIC images pseudocolored
1067 green, and HT-labeled molecules are magenta. Location of lines used to make
1068 kymographs are shown in the time lapse images (yellow dashed lines). For each protein,
1069 the left kymograph was generated from the cell depicted in the time-lapse images.
1070 Numbers (1-3) denote when each image in the time lapse was taken. The other two

1071 kymographs are from cells that are not shown. Calculation of circumferential velocities
1072 from kymographs is described in *Materials and Methods*. Scale bars = 1 μm. (*B*)
1073 Movement patterns of HT-labeled sm molecules. Bars represent the mean relative
1074 frequency of each type of motion. For a given strain or condition, the relative frequencies
1075 of circumferential (red), diffusive (blue), and static (grey) molecules were determined
1076 manually. Frequencies were then averaged over all biological replicates to determine the
1077 mean (error bars represent ± SD). Mean values are indicated above each error bar, and
1078 the total number of molecules analyzed (n) from the number of biological replicates (R)
1079 for each strain is listed below the strain or condition. Circumferentially moving molecules
1080 were defined as molecules moving in one direction for 6 or more frames (at 1 FPS imaging
1081 rate) with a linear velocity ≥ 5 nm/s. Static molecules were defined as molecules not
1082 moving or moving for 6 or more frames with a velocity < 5 nm/s. Diffusive molecules were
1083 defined as molecules that moved, but not in a consistent direction, for 6 or more non-
1084 consecutive frames within a period of 90 s. Full criteria for determining movement patterns
1085 are described in *Materials and Methods*. The expression level of iHT-fusion proteins
1086 relative to the untagged WT level is shown as a percentage under the strain names. iHT-
1087 fusion proteins were expressed solely from native chromosomal loci or with an additional
1088 copy of the gene encoding the iHT-fusion protein at an ectopic site under control of a zinc-
1089 inducible promoter, with 0 or 0.25 mM Zn inducer added. Unpaired t-tests were performed
1090 to compare relative frequencies of motion types. *ns* (nonsignificant); *$P < 0.05$; **$P < 0.01$;
1091 ***$P < 0.001$; ****$P < 0.0001$.

1092 **Fig. 2.** Diffusively moving components of the core PG elongasome did not actively
1093 synthesize PG (blue) in non-midcell regions of exponentially growing pneumococcal cells.

1094 3D-SIM images, where iHT-bPBP2b is red, regions of PBP transpeptidase activity are
1095 blue, and midcell regions include septa of dividing cells and equators of predivisional
1096 daughter cells. Cells were grown in BHI ± 0.3 mM Zn inducer, labeled with a saturating
1097 amount of HT-ligand (500 nM) for 15 min, washed, labeled with 400 μM of the fluorescent
1098 D-amino acid HADA (blue) for 2.5 min, fixed, and imaged as described in *Materials and*
1099 *Methods*. Images are summed from 15 *Z*-plane sections (*Z*-stack) representing a total
1100 depth of 1.875 μm. Percentages indicate the amount of iHT-bPBP2b expressed relative
1101 to the untagged WT bPBP2b$^+$ level (32). (*A*) *iht-pbp2b* (IU15928) and (*B*) *iht-pbp2b* // P_{Zn}-
1102 *iht-pbp2b* (IU16553). Scale bar = 1 μm.

1103 **Fig. 3.** bPBP2b, RodA, and MreC formed a stable complex during active PG
1104 synthesis. Dot plots of (*A*) circumferential velocities and (*B*) circumferential durations of
1105 elongation PG synthesis proteins were determined by sm-TIRFm at 1 FPS. Strains are
1106 the same as in Figure. 1. +Zn indicates 0.25 mM Zn inducer was added. Black and red
1107 lines are median ± interquartile, and mean ± SD are indicated. n = total molecules
1108 analyzed from 2-5 biological replicates. Dotted grey lines indicate the minimum thresholds
1109 for (*A*) velocity (5 nm/s) and (*B*) duration (6 s). A Kruskal-Wallis with Dunn's multiple
1110 comparisons test was used to compare circumferential velocities or circumferential
1111 durations in different strains. *ns* (nonsignificant); $^{**}P < 0.01$; $^{***}P < 0.001$; $^{****}P < 0.0001$.

1112 **Fig. 4.** Circumferential movement of bPBP2b and RodA was independent of FtsZ
1113 treadmilling and reflective of PG synthesis. Sm-TIRFm was performed at 1 FPS on strains
1114 expressing iHT-bPBP2b or iHT-RodA as described in *Materials and Methods*. Dot plots
1115 of circumferential velocities are shown. Black and red lines are median ± interquartile,
1116 and mean ± SD are indicated. (*A*) Both *iht-pbp2b* (black, IU15928) and *iht-pbp2b* P_{Zn}-

1117 *ftsZ*(D214A) (red, IU16091) strains were supplemented with 0.25 mM Zn inducer. (*B*)
1118 IU16056 expresses both iHT-bPBP2b and FtsZ-sfGFP. The treadmilling velocity of FtsZ-
1119 sfGFP filaments (green) and the circumferential velocity of iHT-bPBP2b single molecules
1120 (red) were determined. (*C*) *iht-pbp2b* (black, IU15928) and *iht-pbp2b* Δ*murZ* (red,
1121 IU16110) strains. (*D*) *iht-rodA* (black, IU15970) and *iht-rodA* Δ*murZ* (blue, IU16112)
1122 strains. n = total molecules analyzed from two biological replicates. Circumferential
1123 velocities in different strains were compared using a Mann-Whitney test. **P* < 0.05; *****P*
1124 < 0.0001.

1125 **Fig. 5.** Circumferential movement of aPBP1a reflected active PG synthesis. Sm-
1126 TIRFm was performed at 1 FPS as described in *Materials and Methods* on strains *iht-*
1127 *pbp1a* // P_{Zn}-*iht-pbp1a* (IU16497) and *iht-pbp1a*(S370A) // P_{Zn}-*iht-pbp1a*(S370A)
1128 (IU19168) with 0.25 mM Zn inducer added. Movement patterns of HT-labeled molecules
1129 at sites of PG synthesis (midcell) or elsewhere in the cell (non-midcell) were determined.
1130 The layout is the same as Figure 1*B* (see legend for details). A two-way ANOVA with
1131 Tukey's multiple comparison test was used to compare relative frequencies of motion
1132 types among strains. **P* < 0.05.

1133 **Fig. 6.** Elongation PG synthesis-associated proteins exhibited different patterns of
1134 confined diffusion. Sm-TIRFm was performed at 20 FPS on strains *iht-pbp2b* // P_{Zn}-*iht-*
1135 *pbp2b* (IU16553), *iht-rodA* // P_{Zn}-*iht-rodA* (IU16496), *iht-mreC* (IU16344), *iht-pbp1a* // P_{Zn}-
1136 *iht-pbp1a* (IU16497) and *iht-mpgA* (IU15997) as described in *Materials and Methods*. 0.25
1137 mM Zn inducer was added to strains IU16553, IU16496 and IU16497. Mean square
1138 displacements (MSD) were calculated for diffusive and non-diffusive trajectories. Circles
1139 show MSD values, and error bars represent SEM. Lines represent MSD curves fit to the

1140 data as described in *Materials and Methods*. The MSD curves were compared using a
1141 two-sample Kolmogorov-Smirnov test. *$P < 0.05$; *ns*, nonsignificant. To the right of the
1142 graph are the mean diffusion coefficients (± SEM) of diffusive trajectories, alpha values
1143 of diffusive trajectories (α), the percent of total trajectories that were classified as diffusive
1144 (% diffusive), and the total number of trajectories (n) analyzed from 2 biological replicates.
1145 α values < 1 indicate that molecules exhibited diffusion (or subdiffusion) as discussed in
1146 the text. The diffusion coefficients were compared between strains using a Brown-
1147 Forsythe and Welch's ANOVA with a Games-Howell multiple comparison test. **$P < 0.01$;
1148 *ns*, nonsignificant. See Figure S22 for representative fields of cells containing multiple
1149 single-molecule trajectories.

1150 **Fig. 7.** Summary model of the composition and dynamics of core elongasome
1151 components (bPBP2b, RodA, and MreC) and proteins linked to PG elongation synthesis
1152 (aPBP1a and MpgA) in growing *S. pneumoniae* cells. The circumferential, processive
1153 movement of bPBP2b, RodA, and MreC reported here likely applies to the other core
1154 elongasome components RodZ and MreD, which were not determined in this study. In
1155 early, predivisional cells, the core PG elongasome is located in the FtsZ-ring at the
1156 equator midcell of a daughter cell. In later divisional cells, the core PG elongasome is in
1157 the outer ring of the midcell septal annular disk. The motion of MreC was shown to be the
1158 same in early or late divisional cells. Class A aPBP1a also displays circumferential,
1159 processive motion at midcell that depends on PG synthesis, but its dynamics indicate that
1160 aPBP1a is not a persistent member of the core PG elongasome, although short
1161 interactions are possible. In contrast, MpgA moves in a distinctive type of subdiffusion in
1162 the midcell region. Components of the core elongasome, aPBP1a, and MpgA also move

1163 diffusively outside of midcell rings. There are also nonmoving, static molecules (> 6 s) of
1164 elongasome proteins and aPBP1a, mainly in midcell regions. It is not clear whether static
1165 molecules are synthesizing PG or are in a non-synthesizing transition state (see
1166 *Discussion*). In addition, diffusing molecules of aPBP1a and MpgA were infrequently
1167 detected pausing (< 1s) before resuming motion. See text for additional information.

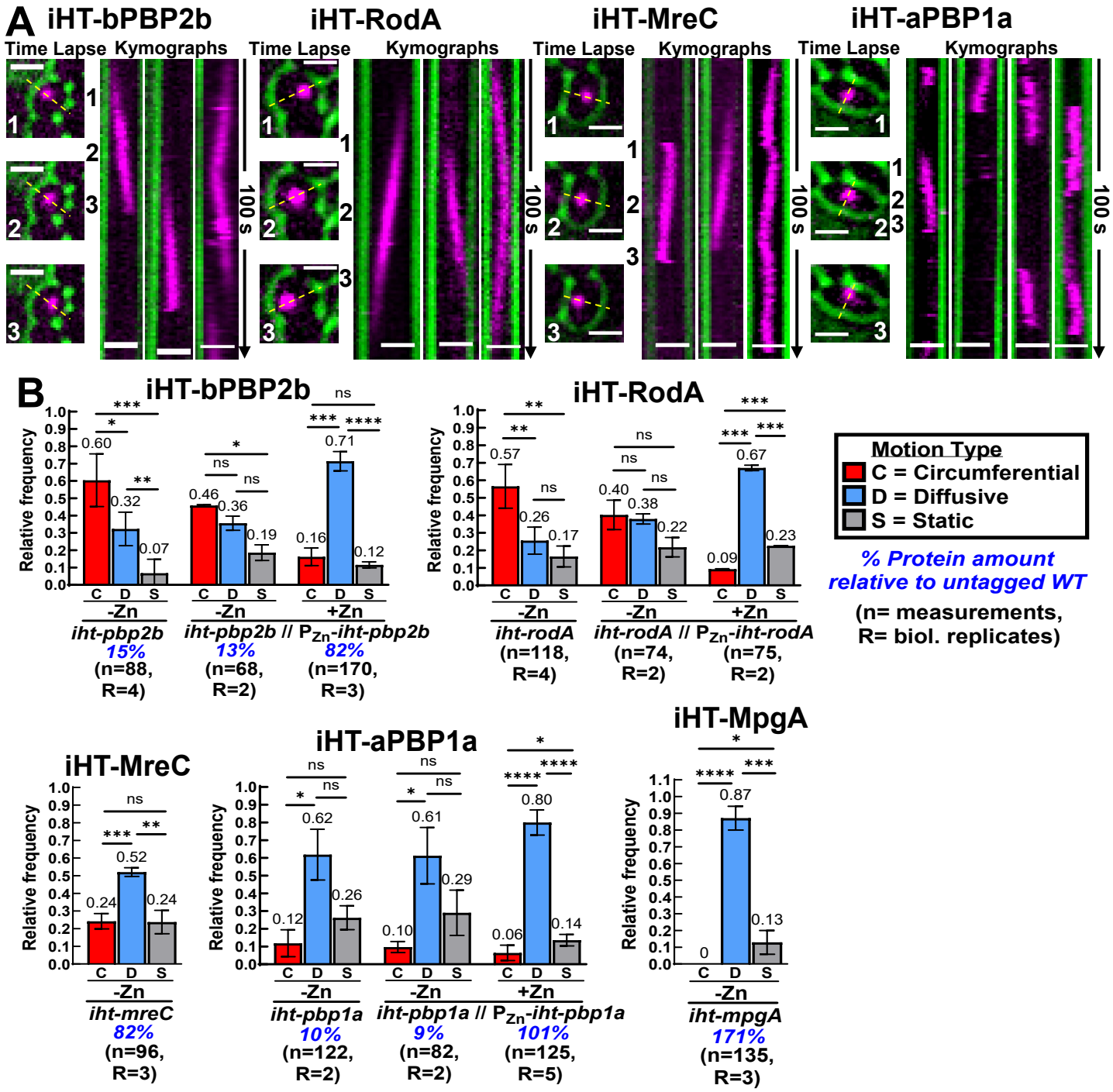
A
iHT-bPBP2b
iHT-RodA
iHT-MreC
iHT-aPBP1a
Time Lapse
Kymographs
100 s
B
iHT-bPBP2b
Relative frequency
0.60
0.32
0.07
0.46
0.36
0.19
0.16
0.71
0.12
-Zn
-Zn
+Zn
iht-pbp2b
15%
(n=88, R=4)
iht-pbp2b // PZn-iht-pbp2b
13%
(n=68, R=2)
82%
(n=170, R=3)
iHT-RodA
0.57
0.26
0.17
0.40
0.38
0.22
0.09
0.67
0.23
iht-rodA
(n=118, R=4)
iht-rodA // PZn-iht-rodA
(n=74, R=2)
(n=75, R=2)
Motion Type
C = Circumferential
D = Diffusive
S = Static
% Protein amount relative to untagged WT
(n= measurements, R= biol. replicates)
iHT-MreC
0.24
0.52
0.24
iht-mreC
82%
(n=96, R=3)
iHT-aPBP1a
0.12
0.62
0.26
0.10
0.61
0.29
0.06
0.80
0.14
iht-pbp1a
10%
(n=122, R=2)
iht-pbp1a // PZn-iht-pbp1a
9%
(n=82, R=2)
101%
(n=125, R=5)
iHT-MpgA
0
0.87
0.13
iht-mpgA
171%
(n=135, R=3)

Fig. 1.

Fig. 1. Elongation PG synthesis proteins displayed processive circumferential motion, and a limited number of molecules simultaneously engaged in PG synthesis. Sm-TIRFm was performed at 1 FPS as described in *Materials and Methods* on strains *iht-pbp2b* (IU15928), *iht-pbp2b* // P_{Zn}-*iht-pbp2b* (IU16553), *iht-rodA* (IU15970), *iht-rodA* // P_{Zn}-*iht-rodA* (IU16496), *iht-mreC* (IU16344), *iht-pbp1a* (IU16320), *iht-pbp1a* // P_{Zn}-*iht-pbp1a* (IU16497), and *iht-mpgA* (IU15997). (*A*) Representative time-lapse images and kymographs of molecules displaying processive circumferential movement in strains IU15928, IU15970, IU16344, and IU16497. Cell outlines are DIC images pseudocolored green, and HT-labeled molecules are magenta. Location of lines used to make kymographs are shown in the time lapse images (yellow dashed lines). For each protein, the left kymograph was generated from the cell depicted in the time-lapse images. Numbers (1-3) denote when each image in the time lapse was taken. The other two kymographs are from cells that are not shown. Calculation of circumferential velocities from kymographs is described in *Materials and Methods*. Scale bars = 1 μm. (*B*) Movement patterns of HT-labeled sm molecules. Bars represent the mean relative frequency of each type of motion. For a given strain or condition, the relative frequencies of circumferential (red), diffusive (blue), and static (grey) molecules were determined manually. Frequencies were then averaged over all biological replicates to determine the mean (error bars represent ± SD). Mean values are indicated above each error bar, and the total number of molecules analyzed (n) from the number of biological replicates (R) for each strain is listed below the strain or condition. Circumferentially moving molecules were defined as molecules moving in one direction for 6 or more frames (at 1 FPS imaging rate) with a linear velocity ≥ 5 nm/s. Static molecules were defined as molecules not moving or moving for 6 or more frames with a velocity < 5 nm/s. Diffusive molecules were defined as molecules that moved, but not in a consistent direction, for 6 or more non-consecutive frames within a period of 90 s. Full criteria for determining movement patterns are described in *Materials and Methods*. The expression level of iHT-fusion proteins relative to the untagged WT level is shown as a percentage under the strain names. iHT-fusion proteins were expressed solely from native chromosomal loci or with an additional copy of the gene encoding the iHT-fusion protein at an ectopic site under control of a zinc-inducible promoter, with 0 or 0.25 mM Zn inducer added. Unpaired t-tests were performed to compare relative frequencies of motion types. *ns* (nonsignificant); $^{*}P < 0.05$; $^{**}P < 0.01$; $^{***}P < 0.001$; $^{****}P < 0.0001$.

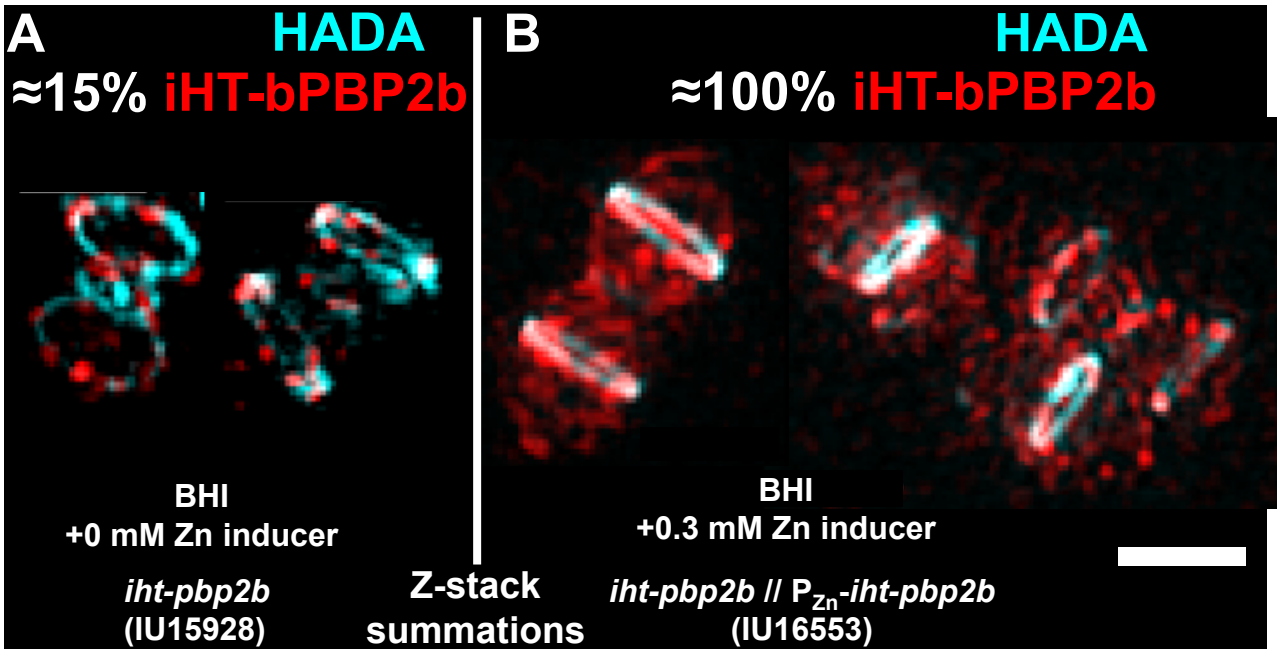

Fig. 2. Diffusively moving components of the core PG elongasome did not actively synthesize PG (blue) in non-midcell regions of exponentially growing pneumococcal cells. 3D-SIM images, where iHT-bPBP2b is red, regions of PBP transpeptidase activity are blue, and midcell regions include septa of dividing cells and equators of predivisional daughter cells. Cells were grown in BHI ± 0.3 mM Zn inducer, labeled with a saturating amount of HT-ligand (500 nM) for 15 min, washed, labeled with 400 μM of the fluorescent D-amino acid HADA (blue) for 2.5 min, fixed, and imaged as described in *Materials and Methods*. Images are summed from 15 *Z*-plane sections (*Z*-stack) representing a total depth of 1.875 μm. Percentages indicate the amount of iHT-bPBP2b expressed relative to the untagged WT bPBP2b^{+} level (32). (*A*) *iht-pbp2b* (IU15928) and (*B*) *iht-pbp2b* // P_{Zn}-*iht-pbp2b* (IU16553). Scale bar = 1 μm.

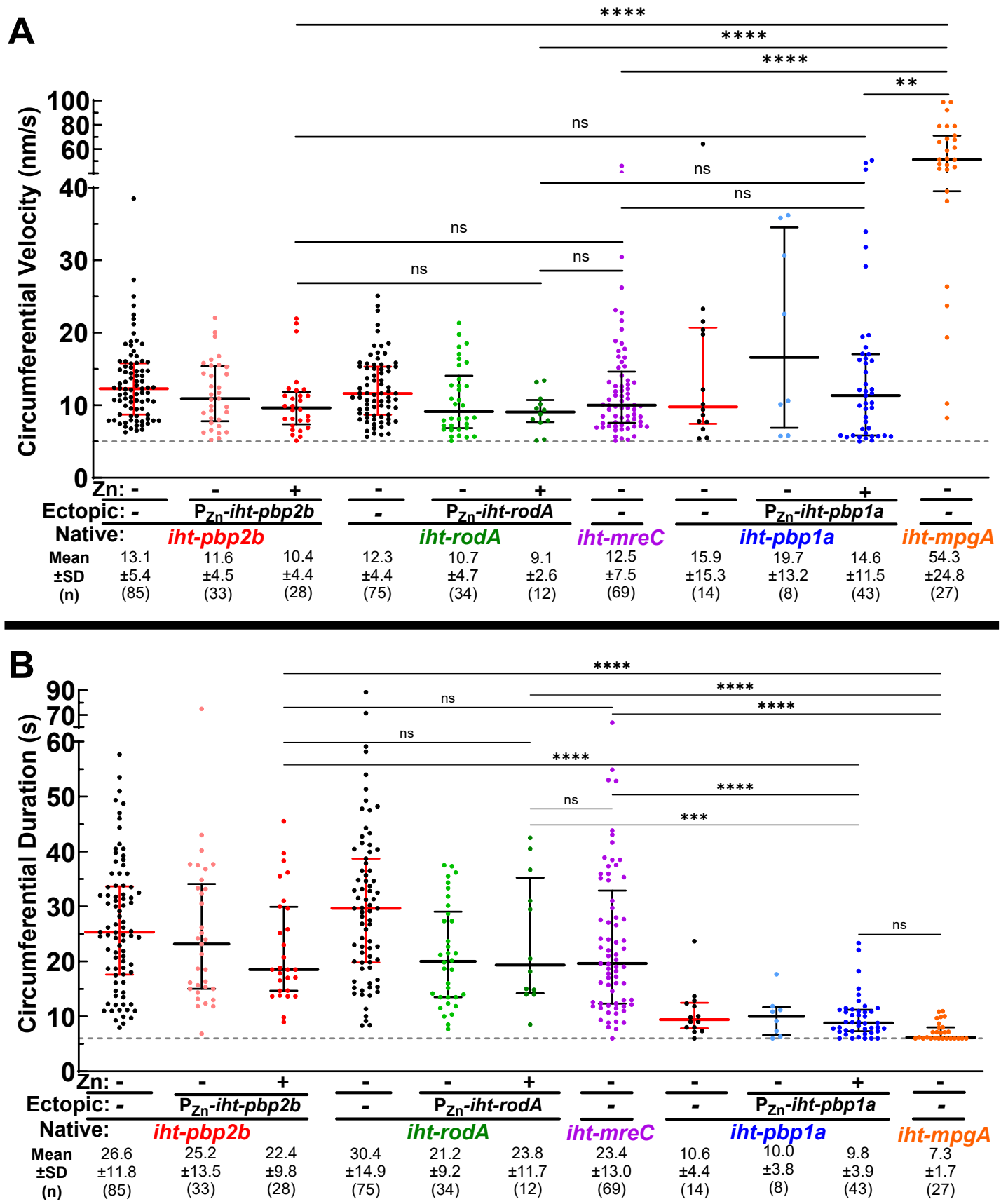
A
Circumferential Velocity (nm/s)
100
80
60
40
30
20
10
0
****
****
****
**
ns
ns
ns
ns
ns
ns
Zn: - - + - - + - - - + -
Ectopic: - P_{Zn}-iht-pbp2b - P_{Zn}-iht-rodA - - P_{Zn}-iht-pbp1a -
Native: iht-pbp2b iht-rodA iht-mreC iht-pbp1a iht-mpgA
Mean 13.1 11.6 10.4 12.3 10.7 9.1 12.5 15.9 19.7 14.6 54.3
±SD ±5.4 ±4.5 ±4.4 ±4.4 ±4.7 ±2.6 ±7.5 ±14.3 ±13.2 ±11.5 ±24.8
(n) (85) (33) (28) (75) (34) (12) (69) (14) (8) (43) (27)
B
Circumferential Duration (s)
90
70
60
50
40
30
20
10
0
****
****
****
ns
ns
****
****
ns
***
ns
Zn: - - + - - + - - - + -
Ectopic: - P_{Zn}-iht-pbp2b - P_{Zn}-iht-rodA - - P_{Zn}-iht-pbp1a -
Native: iht-pbp2b iht-rodA iht-mreC iht-pbp1a iht-mpgA
Mean 26.6 25.2 22.4 30.4 21.2 23.8 23.4 10.6 10.0 9.8 7.3
±SD ±11.8 ±13.5 ±9.8 ±14.9 ±9.2 ±11.7 ±13.0 ±4.4 ±3.8 ±3.9 ±1.7
(n) (85) (33) (28) (75) (34) (12) (69) (14) (8) (43) (27)

Fig. 3.

Fig. 3. bPBP2b, RodA, and MreC formed a stable complex during active PG synthesis. Dot plots of (*A*) circumferential velocities and (*B*) circumferential durations of elongation PG synthesis proteins were determined by sm-TIRFm at 1 FPS. Strains are the same as in Figure. 1. +Zn indicates 0.25 mM Zn inducer was added. Black and red lines are median ± interquartile, and mean ± SD are indicated. n = total molecules analyzed from 2-5 biological replicates. Dotted grey lines indicate the minimum thresholds for (*A*) velocity (5 nm/s) and (*B*) duration (6 s). A Kruskal-Wallis with Dunn's multiple comparisons test was used to compare circumferential velocities or circumferential durations in different strains. *ns* (nonsignificant); $^{**}P < 0.01$; $^{***}P < 0.001$; $^{****}P < 0.0001$.

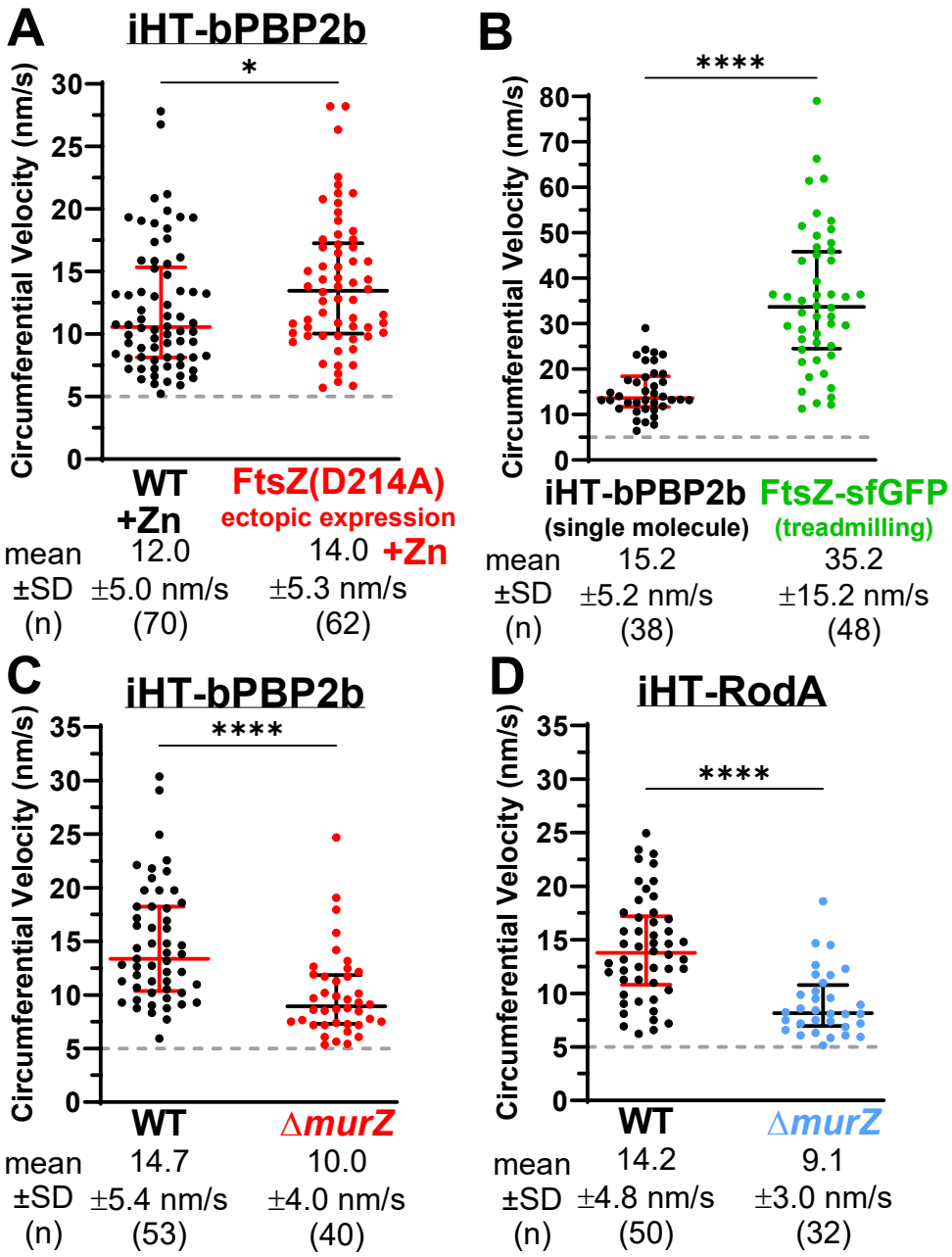

Fig. 4. Circumferential movement of bPBP2b and RodA was independent of FtsZ treadmilling and reflective of PG synthesis. Sm-TIRFm was performed at 1 FPS on strains expressing iHT-bPBP2b or iHT-RodA as described in *Materials and Methods*. Dot plots of circumferential velocities are shown. Black and red lines are median ± interquartile, and mean ± SD are indicated. (*A*) Both *iht-pbp2b* (black, IU15928) and *iht-pbp2b* P_{Zn}-*ftsZ*(D214A) (red, IU16091) strains were supplemented with 0.25 mM Zn inducer. (*B*) IU16056 expresses both iHT-bPBP2b and FtsZ-sfGFP. The treadmilling velocity of FtsZ-sfGFP filaments (green) and the circumferential velocity of iHT-bPBP2b single molecules (red) were determined. (*C*) *iht-pbp2b* (black, IU15928) and *iht-pbp2b* Δ*murZ* (red, IU16110) strains. (*D*) *iht-rodA* (black, IU15970) and *iht-rodA* Δ*murZ* (blue, IU16112) strains. n = total molecules analyzed from two biological replicates. Circumferential velocities in different strains were compared using a Mann-Whitney test. *$P < 0.05$; ****$P < 0.0001$.

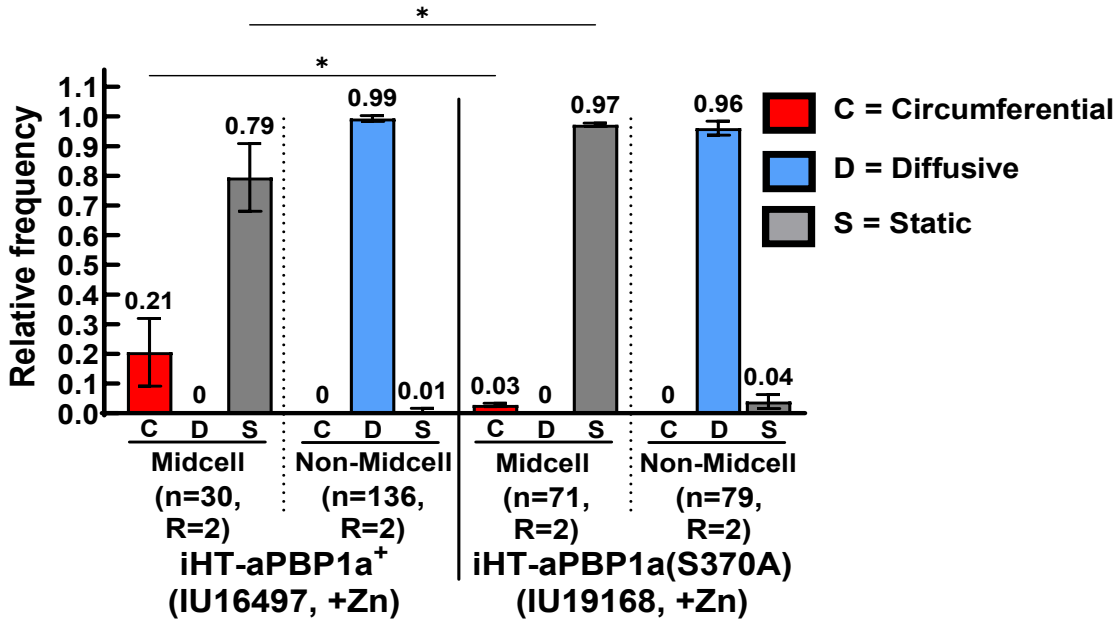

Fig. 5. Circumferential movement of aPBP1a reflected active PG synthesis. Sm-TIRFm was performed at 1 FPS as described in *Materials and Methods* on strains *iht-pbp1a* // P_{Zn}-*iht-pbp1a* (IU16497) and *iht-pbp1a*(S370A) // P_{Zn}-*iht-pbp1a*(S370A) (IU19168) with 0.25 mM Zn inducer added. Movement patterns of HT-labeled molecules at sites of PG synthesis (midcell) or elsewhere in the cell (non-midcell) were determined. The layout is the same as Figure 1*B* (see legend for details). A two-way ANOVA with Tukey's multiple comparison test was used to compare relative frequencies of motion types among strains. *$P < 0.05$.

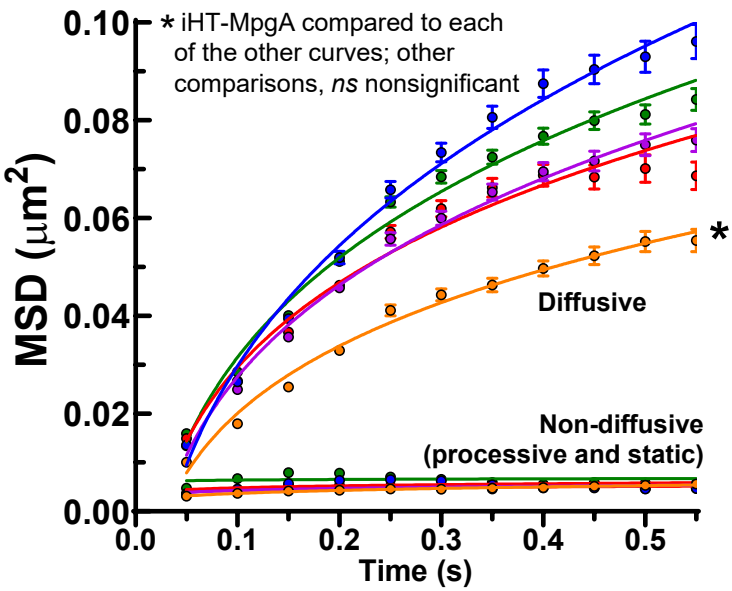

	Protein Diffusion coefficient (μm²/s) ±SEM	α	% Diffusive	n
iht-pbp1a // P_{Zn}-*iht-pbp1a* +Zn	0.055[1] ±0.0005	0.28	77	914
iht-rodA // P_{Zn}-*iht-rodA* +Zn	0.050 ±0.0002	0.23	90	2,116
iht-mreC	0.047 ±0.0003	0.22	68	1,351
iht-pbp2b // P_{Zn}-*iht-pbp2b* +Zn	0.046 ±0.0003	0.20	74	1,143
iht-mpgA	0.040 ±0.0003	0.18	60	1,291

[1] iHT-aPBP1a *vs* iHT-MpgA **; all other comparisons *ns*

Fig. 6. Elongation PG synthesis proteins exhibited different patterns of confined diffusion. Sm-TIRFm was performed at 20 FPS on strains *iht-pbp2b* // P_{Zn}-*iht-pbp2b* (IU16553), *iht-rodA* // P_{Zn}-*iht-rodA* (IU16496), *iht-mreC* (IU16344), *iht-pbp1a* // P_{Zn}-*iht-pbp1a* (IU16497) and *iht-mpgA* (IU15997) as described in *Materials and Methods*. 0.25 mM Zn inducer was added to strains IU16553, IU16496 and IU16497. Mean square displacements (MSD) were calculated for diffusive and non-diffusive trajectories. Circles show MSD values, and error bars represent SEM. Lines represent MSD curves fit to the data as described in *Materials and Methods*. The MSD curves were compared using a two-sample Kolmogorov-Smirnov test. *$P < 0.05$; *ns*, nonsignificant. To the right of the graph are the mean diffusion coefficients (± SEM) of diffusive trajectories, alpha values of diffusive trajectories (α), the percent of total trajectories that were classified as diffusive (% diffusive), and the total number of trajectories (n) analyzed from 2 biological replicates. α values < 1 indicate that molecules exhibited diffusion (or subdiffusion) as discussed in the text. The diffusion coefficients were compared between strains using a Brown-Forsythe and Welch's ANOVA with a Games-Howell multiple comparison test. **$P < 0.01$; *ns*, nonsignificant. See Figure S22 for representative fields of cells containing multiple single-molecule trajectories.

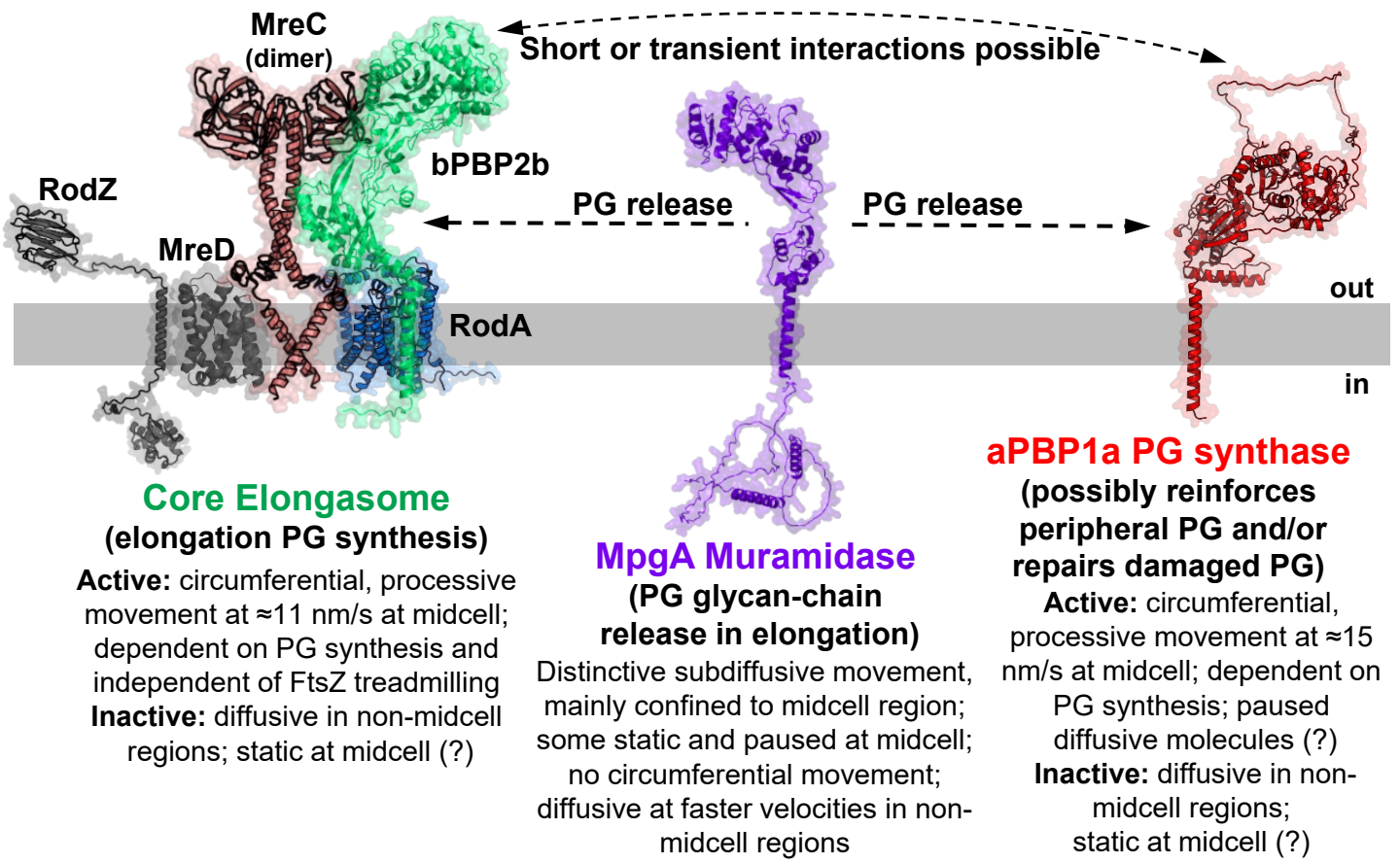

Fig. 7. Summary model of the composition and dynamics of core elongasome components (bPBP2b, RodA, and MreC) and proteins linked to PG elongation synthesis (aPBP1a and MpgA) in growing *S. pneumoniae* cells. The circumferential, processive movement of bPBP2b, RodA, and MreC reported here likely applies to the other core elongasome components RodZ and MreD, which were not determined in this study. In early, predivisional cells, the core PG elongasome is located in the FtsZ-ring at the equator midcell of a daughter cell. In later divisional cells, the core PG elongasome is in the outer ring of the midcell septal annular disk. The motion of MreC was shown to be the same in early or late divisional cells. Class A aPBP1a also displays circumferential, processive motion at midcell that depends on PG synthesis, but its dynamics indicate that aPBP1a is not a persistent member of the core PG elongasome, although short interactions are possible. In contrast, MpgA moves in a distinctive type of subdiffusion in the midcell region. Components of the core elongasome, aPBP1a, and MpgA also move diffusively outside of midcell rings. There are also nonmoving, static molecules (> 6 s) of elongasome proteins and aPBP1a, mainly in midcell regions. It is not clear whether static molecules are synthesizing PG or are in a non-synthesizing transition state (see *Discussion*). In addition, diffusing molecules of aPBP1a and MpgA were infrequently detected pausing (< 1s) before resuming motion. See text for additional information.